Validation of an ultrasound-embedded shoe for calculating stiffness of the plantar soft tissue

Nicholas Reese Ozanich

A thesis

submitted in partial fulfillment of the

requirements for the degree of

Master of Science

University of Washington

2025

Committee:

William R. Ledoux

Michael Bailey

Mehmet Kurt

Daniel Leotta

Program Authorized to Offer Degree:

Mechanical Engineering

University of Washington

Abstract

Validation of an ultrasound-embedded shoe for calculating stiffness of the plantar soft tissue

Nicholas Reese Ozanich

Chair of the Supervisory Committee:

William R. Ledoux

Mechanical Engineering

In the United States, diabetes affects approximately 38.4 million people, or 11.6% of the population, including nearly 29% of adults aged 65, and older and can lead to foot complications such as peripheral neuropathy and ulceration. Quantifying tissue-level structural changes due to diabetes may improve our understanding of ulcer formation. This work focused on the Ultrashoe, a device that integrates an ultrasound sensor and load cells to assess plantar soft tissue mechanics. To calculate stiffness, the Ultrashoe must accurately measure both force and displacement. The most accurate speeds of sound for the plantar tissue were identified as 1600 m/s for the heel and 1660 m/s for the second metatarsal head. Load cell error was found to be acceptable. In cadaver testing, stiffness increased with loading frequency and decreased with higher assumed sound speed. This work represents an important validation step toward using the Ultrashoe to study diabetes-related structural changes in the foot and to explore its potential integration with plantar pressure measurements to investigate the effect of diabetes in the foot.

Table of Contents

Acknowledgements

I am deeply grateful for the opportunity to work on this project over the past nine months and for the many people who have supported my academic journey in the field of biomechanics. My initial interest in biomechanics started working with Dr. David Lin and Dr. Anita Vasavada at Washington State University. Their mentorship laid the foundation for my interest in research and pursuing biomechanics as a field. At the University of Washington, I had the privilege of working with Dr. Cristine Agresta, whose projects introduced me to the use of ultrasound in biomechanics research, an area that immediately resonated with me and shaped the direction of my academic focus. This experience led directly to my involvement at the Center for Limb Loss and MoBility (CLiMB), which has been an incredibly rewarding opportunity. Working with the research engineers and under the mentorship of my advisor, Dr. William Ledoux, has allowed me to grow more as a researcher in one year than I ever anticipated and has deepened my appreciation for biomechanics research.

I would also like to thank my classmates, friends, and family for their ongoing encouragement and belief in my personal and professional development. The past year has been filled with growth in many different ways and the support from everyone has made this journey all the more meaningful and fulfilling.

Introduction

Diabetes

Diabetes is a major public health challenge, affecting approximately 537 million adults globally as of 2021 [1]. In the United States, diabetes affects about 38.4 million people, or 11.6% of the population, including nearly 29% of adults aged 65 years or older [2]. In 2022, the U.S. healthcare system spent approximately $413 billion on diabetes-related care, accounting for roughly one in every four dollars spent on healthcare [3]. Diabetes also disproportionately affects historically marginalized groups in the United States, with significantly higher prevalence rates among American Indian/Alaska Native (13.6%) and non-Hispanic Black (12.1%) populations compared to non-Hispanic White adults (6.9%) [2]. In addition to racial and ethnic disparities in the United States, diabetes prevalence varies significantly across different socioeconomic groups, with 13.1% of adults with less than a high school education, 9.1% with those who have a high school education, and 6.9% for those with more than a high school education [2]. Furthermore, U.S. Veterans are significantly predisposed to developing diabetes, with approximately one in four individuals receiving care from the Veterans Health Administration (VHA) affected [4].

Clinically, diabetes is diagnosed through measures of hyperglycemia, including elevated fasting plasma glucose (≥126 mg/dL) or hemoglobin A1c (≥6.5%) [5]. Prediabetes describes a state in which glucose levels are elevated but have not yet surpassed diabetic thresholds (fasting plasma glucose between 100 mg/dL and 125 mg/dL or A1C range of 5.7-6.4%) [5]. During this phase, individuals may exhibit no noticeable symptoms despite ongoing metabolic stress. Prolonged exposure to elevated glucose, even at prediabetic levels, significantly increases the risk of

cardiovascular diseases such as heart disease and stroke [5]. Currently, approximately one in three U.S. adults live with prediabetes [2]. Diabetes represents a substantial source of metabolic stress on a significant portion of people globally and is a leading contributor to long-term complications such as cardiovascular disease and neuropathy. Its chronic nature requires ongoing management and places a considerable burden on healthcare systems, particularly as prevalence continues to rise in both developed and developing countries.

The development of type 2 diabetes is driven by both genetic and lifestyle factors. Major contributors include obesity and physical inactivity, which promote insulin resistance, along with family history, aging, and other systemic stressors like tobacco use and alcohol consumption [5]. Chronic diabetes affects multiple organ systems through the damaging consequences of sustained hyperglycemia and associated metabolic disturbances. For instance, prolonged hyperglycemia may cause microvascular injuries resulting in retinopathy (retinal damage potentially leading to vision loss), nephropathy (kidney damage possibly culminating in kidney failure), and neuropathy (nerve damage leading to pain or sensory loss) [5]. Despite extensive documentation of diabetes-related risk factors and complications, the disease remains extremely prevalent both in the United States and globally.

Preventive measures for diabetes are largely rooted in lifestyle choices, particularly emphasizing physical activity, dietary habits, and weight management. Engaging in regular exercise and maintaining a balanced diet have been widely recognized as effective strategies for preventing diabetes and reducing related risk factors [5]. The Diabetes Prevention Program trial demonstrated that intensive lifestyle modifications, including structured physical activity and dietary counseling,

reduced the incidence of diabetes by approximately 58%, with sustained benefits observed for over a decade [5]. Despite these promising results, implementing and sustaining intensive lifestyle changes can be challenging, highlighting the need for supplementary approaches.

Metformin, a medication commonly prescribed for managing high blood glucose levels unrelated to type 1 diabetes, may be considered as a preventive measure for individuals at elevated risk for type 2 diabetes. It is particularly recommended for adults aged 25–59 years who have a body mass index (BMI) greater than or equal to 35 kg/m², elevated fasting plasma glucose (≥110 mg/dL), elevated hemoglobin A1c (≥6.0%), or a history of gestational diabetes mellitus [5]. However, Metformin was notably less effective compared to intensive lifestyle interventions, underscoring the primary importance of lifestyle modifications as the foundation for diabetes prevention [5].

In recent years, glucagon-like peptide-1 receptor agonists (GLP-1 RAs) have emerged as promising pharmacological interventions. Originally developed for diabetes and obesity management, these drugs have gained widespread attention in recent years. Clinical studies have consistently demonstrated that GLP-1 RAs, particularly when paired with lifestyle modifications, effectively lower both hemoglobin A1c levels and body weight without significantly increasing the risk of hypoglycemia [6]. The FDA has approved several GLP-1 drugs explicitly for the management of both obesity and type 2 diabetes [5]. Nonetheless, GLP-1 RAs are already strongly recommended by the American Diabetes Association (ADA) to reduce A1c levels where necessary [5]. However, they are a relatively new class of drug where variations of GLP-1 RAs have been steadily gained FDA approval since the first successful GLP-1 RA, exenatide, was approved by the FDA in 2005, which was administered twice daily. Further innovation led to GLP-1 RAs that

can be administered weekly, improving patient adherence [7]. This class of drugs proves to be a transformative advancement in diabetes and obesity management and will is likely to be a key factor in addressing one of the most pressing health challenges of modernity.

In summary, diabetes presents substantial challenges due to its high prevalence and significant burden it places on healthcare systems. While both lifestyle and pharmacological interventions have demonstrated effectiveness, diabetes remains a major disease impacting millions of individuals each year. Complications such as peripheral neuropathy and foot ulceration are well-documented consequences that impair mobility and quality of life. However, despite extensive study, there is still much to uncover about the mechanisms through which diabetes contributes to neuropathy and foot ulceration. Although structural deformity is associated with risk of ulceration [8], [9], the specific mechanisms driving ulcer development remain poorly understood. There is a structural hypothesis for ulcer formation [10], [11], yet methods to assess this are typically limited to clinical comorbidities and plantar pressures [8], [12]. Advancing the ability to quantify tissue-level structural changes due to diabetes continues to be a critical area of research in understanding in preventing ulcer formation.

The effects of diabetes in the foot

Diabetes mellitus can lead to a variety of detrimental changes in foot tissues. The plantar soft tissue of the foot is structurally diverse, composed of skin, subcutaneous fat pads (varying in size and biomechanical function), fascia, tendons, muscle, and ligaments. Collectively, these tissues provide essential shock absorption and distribute loads, reducing the impact of ground reaction

forces experienced during gait and daily activities. Degradation of these tissues, due to diabetes, can alter the foot's function and can lead to serious complications such as foot ulcers or amputation [13]. The calcaneus is the largest bone in the foot and is the place where the calcaneal tendon, more commonly known as the Achilles tendon, attaches on the inferior posterior side of the bone and the plantar ligament attaches at the tuberosity to almost the anterior end of the bone [14]. The heel pad protects the calcaneus during gait and is a common location of ulceration [15]. The heel pad is structurally unique and is vital for protecting the posterior bones in the foot via dissipating forces experienced from ground contact during the stance phase of gait. The plantar fat pad is predominantly divided into two structures of the deep macrochambers and superficial microchambers. The macrochambers consist of large chambers of relatively equal amounts of collagen and elastic fibers while the microchambers are predominantly elastic chambers [16]. The difference in composition leads to different mechanical functions. The macrochambers contribute to the heel's ability to cushion loads and recover after deformation, while the stiffer microchambers help prevent excessive deformation of the macrochamber tissue and contain it underneath the calcaneus [17]. It has also been demonstrated that compared to healthy subjects, diabetic subjects had significantly reduced microchamber stiffness and increased macrochamber stiffness [17]. The decrease in microchamber stiffness was thought to result in reduced capability of confining the macrochambers while the increase in macrochamber stiffness was hypothesized to be a degradation in the ability to cushion loads and recover after deformation which results in transferring more loads to the skin from the calcaneus. They also suggested that diabetes may alter the plantar heel soft tissue structures after about seven years, though some subjects had abnormalities with only five months of disease duration. Additionally, the metatarsal heads, places of bony prominence, are also locations in which ulceration is common [15]. The plantar tissue

under the metatarsal heads is composed of intrinsic muscles, a flexor digitorum longus tendon, fat compartments and ligaments.

Chronically elevated blood glucose can cause the formation of advanced glycation end products (AGEs) which accumulate in connective tissues. This results in abnormal collagen cross-linking and a loss of elasticity in tissue [18], which leads to stiffer tissues and limited joint mobility. Additionally, diabetes-induced peripheral neuropathy and microvascular disease impact sensation and blood flow, respectively, creating an environment where even minor injuries have a worsened ability to heal [18]. Approximately 85% of diabetes-related lower extremity amputations are preceded by a foot ulcer that failed to heal [19]. These ulcers often result from the combined effects of neuropathic loss of protective sensation and biomechanical stresses on stiff, insensate tissues.

A notable change in the diabetes foot is the atrophy of the intrinsic foot muscles. Diabetic peripheral neuropathy leads to the degradation of the small muscles of the foot, which weakens the support of the arch and alters gait dynamics. These causes are sources of increased plantar pressure on areas like the metatarsal heads [20]. The combined risk of increased magnitude of plantar pressures combined with the loss of sensation elevates the risk of tissue degradation and ulcer formation. The plantar fat tissue beneath the metatarsal heads also undergoes degradation. One explanation is that the non-enzymatic glycation of proteins in the fat pad's fibrous septa causes an irregular collagen arrangement and shrinking of fat cells [21]. Another theory is that the fat pad in diabetic subjects shifts away from the metatarsal heads, leaving bony prominences less protected. Without the protection of the fat pad, the metatarsal heads experience greater pressures

and are thereby more prone to ulceration. Likely, these are both contributing factors to the loss of effective cushioning in the diabetic forefoot.

Diabetes is also associated with structural changes in the foot, leading to abnormally thickened plantar fascia and Achilles tendon in diabetic individuals. One study utilizing ultrasound and shear wave elastography found increased Achilles tendon thickness and a reduction in shear wave speed, indicated decreased stiffness in diabetic subjects [22]. Another study by the same research group used ultrasound and strain elastography on the plantar fascia and found that people with diabetes had thicker and less stiff plantar fascia [23]. Similarly, a separate group used weightbearing computed tomography and found that subjects with concurrent neuropathy and claw toes had thicker plantar aponeurosis [24]. The loss of sensation from peripheral neuropathy and the tissue-level changes from the influence of increased chronically elevated glucose levels both contribute to the development of ulcers. However, investigating the structural and mechanical changes due to diabetes likely is not a substitute for current tests for peripheral neuropathy like monofilament testing [25].

Peripheral neuropathy, affecting approximately half of long-term diabetic patients, exacerbates the risk of ulceration by diminishing protective sensation in the foot [26]. This sensory loss often leads to altered foot biomechanics, abnormal gait patterns, and structural deformities which collectively alter plantar pressures and increase the risk for skin breakdown and ulceration [13]. Due to these biomechanical alterations, diabetic individuals may fail to perceive repetitive trauma and prolonged pressure on vulnerable areas, escalating the likelihood of the development of foot ulcers [13].

Given the severity and prevalence of diabetic foot ulceration, clinical strategies commonly focus on reducing peak plantar pressures and redistributing load away from regions prone to repetitive trauma, such as the metatarsal heads using footwear or insoles [27]. However, a major limitation lies in the lack of demonstration that these efforts are effective in preventing a first foot ulcer or heal ischemic or infected ulcers [27]. Foot ulceration is a major complication associated with diabetes mellitus, carrying significant morbidity, mortality, and substantial financial costs to both patients and healthcare systems. The lifetime incidence of diabetic foot ulceration ranges from 19% to 34%, with an annual incidence rate of around 2% [8]. Even after successful healing, recurrence rates remain high, approximately 40% within one year and up to 65% within three years, highlighting the paramount importance of effective prevention strategies [27]. Research into pressure redistribution and effective offloading interventions remains a dynamic and critical field of inquiry for reducing the prevalence and impact of foot ulceration, however as stated previously, current interventions are not demonstrably successful in preventing the development of a first ulcer. There is a need for local measurements of the plantar soft tissue that are more sensitive to the structural and mechanical changes that occur due to diabetes and translating these into effective interventions such as patient-specific orthoses.

Several practical and methodological considerations arise when attempting to redistribute plantar pressures effectively. These considerations include: (1) methodological approaches to analyzing plantar pressure data (e.g., peak pressures, cumulative loading, and pressure-time integral); (2) translating pressure data from research settings into actionable recommendations for commercial or custom-designed footwear or insoles; and (3) the growing field of customized insoles designed

to address individual patient biomechanics and foot morphology [28]. A notable limitation in plantar pressure analyses is that these metrics exclusively measure normal (vertical) forces, neglecting the effect of shear forces. Emerging evidence hypothesizes that shear stresses significantly contribute to skin breakdown and ulcer formation, yet current methodologies for capturing and quantifying shear forces remain limited in clinical practice, largely inhibited by the lack of a commercial shear sensor [12].

Although structural deformities, loss of protective sensation, limited joint mobility, and abundant callus formation seem to correspond with elevated ulcer risk [8], [9], ulcers can sometimes develop independently of peripheral neuropathy or overt structural abnormalities [12]. Despite clinical efforts that use comorbidities and plantar pressures to evaluate ulceration risk, the underlying biomechanical and biological mechanisms driving ulcer formation remain incompletely understood. Most prior research has emphasized biochemical changes, tissue mechanics, and gait alterations associated with diabetes [5], [29]. However, direct investigations into the tissue-level structural changes remain scarce, partly due to methodological challenges in accurately quantifying soft tissue structure and mechanics in vivo.

Medical imaging is a rapidly advancing field and offers valuable opportunities for investigating complications associated with the diabetic foot. Among available modalities, ultrasound imaging stands out as a particularly promising tool due to its accessibility, speed, cost-effectiveness, and strong soft tissue contrast. These attributes make it well-suited for exploring the structural and mechanical changes that occur in diabetic foot tissue. Advanced ultrasound techniques, including three-dimensional imaging and elastography, have the potential to yield detailed information about

tissue stiffness, elasticity, and overall structural integrity [30]. Continued development and refinement of these ultrasound approaches for plantar tissue analysis may greatly enhance our ability to understand how ultrasound-derived measures of tissue quality measures relates to increased plantar pressures and the risk of ulceration.

Imaging the foot

Several medical imaging modalities are commonly employed to assess foot health, each with distinct advantages and limitations (Table 1). X-rays are useful for identifying bone deformities such as fractures or joint misalignments, but poor soft tissue resolution limits their utility in assessing subtle changes in tissue composition. Radiography has been used to characterize plantar fasciitis via plantar fascia thickening, irregularities in bone, and abnormalities in the fat pad beneath the plantar fascia [31]. However, it should not be the first imaging modality of choice for the foot, unless there are suspected bone complications such as stress factors, for example. Computed tomography (CT) offers improved spatial resolution and the ability to generate three-dimensional reconstructions of the foot bones, allowing for more detailed assessment of bony structures and some soft tissue features. However, both X-ray and CT imaging involve exposure to ionizing radiation, which may be a concern for repeated use.

Modality	Best For	Strengths	Limitations
X-ray	Bones, fractures, joint alignment, structural deformities	Quick, low-cost, widely available, excellent for bone detail	Limited soft tissue detail, radiation exposure
CT (computed tomography)	Complex bone structures, subtle fractures, cross-sectional anatomy	High-resolution bone imaging, good for surgical planning	Higher radiation dose than X-ray, limited soft tissue contrast

MRI (magnetic resonance imaging)	Soft tissues, tendons, ligaments, muscles	Superior soft tissue contrast, no radiation	Expensive, time-consuming, sensitive to motion
Ultrasound	Soft tissues, muscles, tendons, superficial structures, real-time imaging	Safe, portable, inexpensive, real-time dynamic imaging	Operator-dependent, limited depth penetration, not ideal for bones or deep tissues

Table 1: Comparison of medical imaging modalities.

Magnetic resonance imaging (MRI) is particularly well-suited for evaluating the plantar soft tissue structures of the foot, including ligaments, tendons, and the plantar fat pad [32]. Its high spatial and contrast resolution allows for detailed visualization of soft tissue composition, making it the preferred modality for detecting pathology such as tendonitis, plantar fasciitis, and ligament tears. MRI is also useful for detecting subtle inflammatory changes, such as those present in early Charcot neuroarthropathy or infection, which may not be visible on other imaging modalities [33]. MRI is unmatched in its spatial resolution for static imaging, but the primary drawbacks are due to the cost, limited availability, and long acquisition times.

Ultrasound, by contrast, is widely available, cost-effective, and portable, making it one of the most commonly used modalities for real-time soft tissue assessment and well-suited for dynamic applications [34]. It does not involve radiation and allows for bedside evaluations and field imaging with newer, portable ultrasound probes which can be connected to mobile phones or tablets. Importantly, ultrasound encompasses a range of techniques suited to different diagnostic needs, including B-mode, Doppler, and elastography imaging, each with its own clinical applications.

In summary, ultrasound offers a unique combination of advantages that make it particularly well-suited for imaging the foot. Unlike X-ray and CT, it does not involve exposure to ionizing radiation, making it safer for repeated use. While MRI provides excellent soft tissue detail, its high cost, limited accessibility, and long scan times reduce its practicality for routine or dynamic assessment. Ultrasound, on the other hand, is portable, cost-effective, and capable of real-time imaging, enabling both static and dynamic evaluations of plantar soft tissues. Its versatility across imaging modes makes it an adaptable tool for studying a range of diabetic foot complications. These qualities position ultrasound as a valuable modality for both clinical assessment and research focused on understanding tissue-level changes associated with ulceration risk and other diabetes-related foot conditions.

Ultrasound physics

Ultrasound imaging operates by transmitting high-frequency sound waves into the body using a transducer, which also receives echoes reflected from internal structures [34]. These echoes are processed to form images based on the time it takes for sound waves to return and the strength of the reflected signal. A fundamental relationship in ultrasound imaging is the equation:

$$d = c * t/2$$

where c is the assumed speed of sound in tissue (typically assumed to be 1540 m/s for soft tissue) and t is the time-of-flight (i.e., time for the sound wave to be transmitted, reflected off a structure, and return to the transducer) [34]. Inaccuracies in the assumed speed of sound can affect spatial measurements, particularly when imaging tissues with differing acoustic properties (e.g., biological tissue). Assuming a speed of sound that is close to the value for one structure with a

known speed of sound may distort other structures with different speeds of sound. For example, if the ultrasound system assumes a speed of 1540 m/s (the standard for soft tissue), it may accurately display structures like muscle (which has a speed of sound of ~1585 m/s) but misrepresent the location or shape of adjacent fat, which has a lower speed of sound (~1440 m/s) [30] or skin (which has a speed of sound of ~1642 m/s [35]. This discrepancy can lead to depth miscalculations, structures in fat may appear thicker than they are, resulting in geometric distortion or measurement errors. Such distortions are particularly relevant in quantitative imaging or when comparing ultrasound data with other imaging modalities like MRI or CT.

Another important concept in ultrasound imaging is attenuation, or the gradual loss of sound wave energy as it travels through tissue. Attenuation occurs due to absorption, scattering, and reflection of the ultrasound beam, and it varies significantly across different tissue types [34]. Higher frequency ultrasound waves provide greater resolution for structures close to the probe, but due to attenuation, they have worse penetration compared to lower frequency ultrasound waves. For example, fat attenuates ultrasound more than muscle or fluid, resulting in decreased signal intensity and reduced image brightness in deeper regions. This variation in attenuation contributes to differences in image quality and must be considered when performing both diagnostic evaluations and quantitative measurements.

In B-mode (brightness mode) ultrasound, what we visualize is the echoes generated by differences in acoustic impedance between adjacent tissues. These impedance differences are largely driven by variations in tissue density and speed of sound. When an ultrasound wave encounters an interface between two tissues with different acoustic properties, such as soft tissue and bone, a

significant portion of the sound wave is reflected back to the transducer. Bone has a much higher acoustic impedance and speed of sound (approximately 2800–4000 m/s) compared to soft tissue (around 1540 m/s). As a result, the interface reflects almost all the incoming ultrasound energy, preventing the wave from penetrating beyond the bone. This creates a characteristic acoustic shadow behind the bone, where no further echoes are received, and the region appears dark on the image. This effect is also observed at interfaces with air, where nearly total reflection occurs due to a large impedance mismatch, which is why a coupling material (e.g., gel or gel pad) is necessary to eliminate air gaps between the probe and skin.

Ultrasound imaging is a versatile tool for examining biological tissues and is widely used due to its accessibility, cost-effectiveness, and real-time capabilities. Conventional B-mode ultrasound provides two-dimensional grayscale images of soft tissue, allowing assessment of tissue thickness and gross structural changes, but it does not measure mechanical stiffness, which can serve as a biomarker for tissue integrity and function. To fill this gap, two primary elastography modalities have been developed: strain elastography and shear wave elastography (SWE).

In strain elastography, an external force, typically compression applied with the ultrasound probe, induces tissue deformation, and the relative displacement within the tissue is tracked to generate a qualitative or semi-quantitative strain map [36], [37]. Stiffer tissues deform less under the same load, making strain elastography useful for detecting local variations in stiffness and identifying local areas of stiffening or softening. Although strain elastography does not directly provide an absolute modulus, pairing measured strains with measured external forces during loading (using devices such as hand-held force gauges or materials testing machines) can yield approximate

elastic modulus values, offering a potential bridge to conventional mechanical testing. This post-hoc approach, not available on most clinical scanners, also aligns well with traditional biomechanical analyses and can be applied dynamically by continuously capturing B-mode images during tissue deformation.

SWE by contrast, uses focused acoustic radiation force to generate shear waves in tissue and measures the propagation speed of those waves [37]. The shear modulus G is estimated from shear wave speed v_s and tissue density ρ via:

$$G = \rho {v_s}^2$$

To convert to the more commonly referenced Young's modulus E, the relationship

$$E = 2G(1 + \nu)$$

where ν is Poisson's ratio (typically assumed to be 0.49 for soft tissue). SWE yields quantitative, depth-resolved stiffness estimates, but it requires a push pulse followed by multiple tracking lines and several seconds of transducer stability to allow readings to stabilize, making it poorly suited to dynamic conditions such as walking.

Ultrasound elastography in the foot

Several studies have used strain elastography to investigate dynamic plantar foot behavior under load [30]. Cyclic loading protocols enable evaluation of stiffness, energy loss (hysteresis), and strain-rate dependence, while constant loading or displacement protocols assess creep or stress relaxation. Strain elastography's adaptability to both dynamic and static loading makes it

particularly well suited to the anatomical and mechanical complexity of plantar soft tissue, enabling capture of physiologically relevant behavior in real-world scenarios.

In this context, stiffness, calculated from applied force and resulting deformation (for example, change in tissue thickness), is the primary elastic property of interest, offering greater interpretability and cross-disciplinary relevance than shear wave-derived metrics. Investigating hysteresis, the energy loss between loading and unloading curves, provides insight into viscoelastic damping properties vital to plantar tissue that undergoes repeated gait cycles. Quantifying hysteresis reflects the tissue's capacity to dissipate energy and may illuminate the effects of diabetes and neuropathy in the foot.

Given the cyclic and dynamic nature of foot loading, both stiffness and hysteresis, as well as strain-rate sensitivity, are hypothesized to be critical parameters for characterizing plantar soft tissue behavior. The ability to measure these properties in vivo using ultrasound represents a significant advance in foot biomechanics research, enabling novel investigations into how elastic and viscoelastic tissue properties relate to foot function, performance, and the progression of pathologies such as diabetic foot complications or age-related tissue degradation.

Specific aims and prior work

SA1: Statically validate ultrasound distance measurements and determine the optimal speed of sound

Motivation: Changing the assumed speed of sound during image acquisition alters the calculated distances, so it is critical to identify the value that minimizes error in plantar tissue.

Relevant prior work

One investigation used CT to validate ultrasound measurements of quadriceps muscle thickness in critically ill patients with acute kidney injury [38]. They found that ultrasound precision was slightly lower than CT but still acceptable. However, they did not report what speed of sound they used, and their CT and ultrasound scans were performed up to 12 hours apart, likely with the default 1540 m/s setting, since many clinical scanners do not allow adjustment. A second study validated articular cartilage thickness against contrast-enhanced micro-CT [39]. Using a 20 MHz A-mode probe on bovine and porcine cartilage-bone plugs, they measured at both the machine's native setting (1580 m/s) and an adjusted value (1696 m/s) from prior acoustics research. Both speeds agreed with micro-CT within 0.1 mm, though the native setting yielded slightly lower error. A third study compared ultrasound to MRI for measuring anterior thigh muscle, subcutaneous adipose tissue, and fascia thickness [40]. They reported high intra-class correlation for muscle and fat measurements but poor agreement for perimuscular fascia. Finally, a deep-learning approach has been applied to estimate spatially varying speed of sound from ultrasound RF data in a dual-modal photoacoustic/ultrasound system [41]. Although aimed at improving photoacoustic

reconstruction, this method could also inform how speed of sound variations affects conventional ultrasound image quality.

SA2: Validate load cell performance in multiple configurations

Motivation: To calibrate the load cells against a reference standard (an Instron materials testing machine) and to quantify any time delay between applied load and measurement by the Ultrashoe sensors.

Relevant prior work

The previous iteration of the Ultrashoe incorporated four Honeywell Model 13 subminiature load cells into its framework and validated them both statically, by applying known weights to the combined load cell and probe assembly and comparing readings against a pressure sensor, and dynamically with a short, simulated walking trial [42]. Since the shoe design and its components have changed, the current validation will re-evaluate the load cell performance in the upgraded Ultrashoe. We will compare the load cell readings directly against an Instron machine, which provides precise, traceable loads, to ensure accuracy and confidence in the measured forces.

SA3: Combine ultrasound and load cells with cadaveric feet to calculate stiffness

Motivation: To demonstrate that the Ultrashoe can accurately measure both displacement and load in series, and to use those data to compute stiffness of the plantar soft tissue.

Relevant prior work

The original Ultrashoe platform was adapted from a commercial training shoe housing an ultrasound probe to assess orthotic inserts [43]. Subjects walked in matched shoes, one with a probe and the other with a Pedar-X® in-shoe pressure sensor; this setup yielded stress–strain curves by pairing contralateral pressure data with ultrasound deformation measurements, but the two signals were not recorded simultaneously. The next iteration replaced the contralateral sensor with four Honeywell Model 13 subminiature load cells arranged in parallel in series with the ultrasound probe [42]. This version was 3D-printed in a mixture of Tango Black Plus resin and Digital ABS Plus Ivory resin, offered finer geometric control, and used a custom-unhoused ultrasound probe; the main drawback was the stiff nature of the shoe being uncomfortable and there were concerns about having diabetic subjects wearing them during walking. The most recent iteration, which is the focus of this thesis, builds on additive manufacturing but employs molded components and a more pliable sole with neoprene straps to improve comfort and was produced in multiple sizes to accommodate different feet.

Methods

The Ultrashoe

The Ultrashoe (Figure 1) is composed of several custom-molded 60A urethane rubber (Simpact, Macungie, PA) and 3D-printed components designed to integrate measurement instrumentation while maintaining a functional shoe form. The primary structure consists of the main body of the shoe, which includes cavities in both the hindfoot and forefoot regions. These recessed areas accommodate the placement of ultrasound probes and load cells, enabling targeted measurement of the heel and second metatarsal head during gait. Within these cutouts, molded insert components are fitted to hold the instrumentation securely. These inserts extend laterally from the shoe, allowing the cables from the ultrasound probe and load cells to exit on the side, thereby minimizing interference with natural foot motion and reducing the likelihood of entanglement during walking.

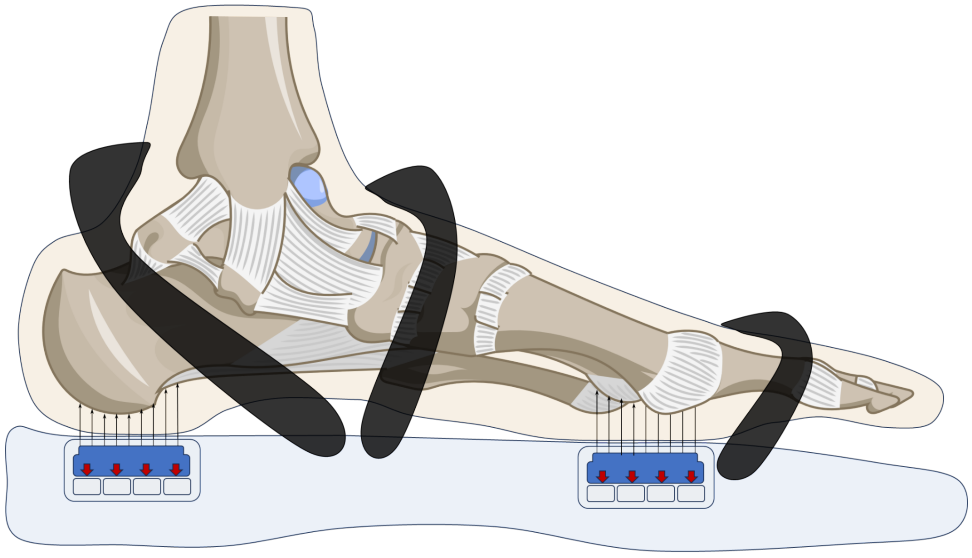

Figure 1: Graphical illustration of the Ultrashoe and its sensors. Original image from the Database Center for Life Science (DBCLS) was adapted to depict skin (tan) as well as the Ultrashoe platform (light blue), the ultrasound probe (dark blue) and its measurement of distance (superiorly pointing black arrows), the four load cells (boxes underneath the ultrasound probe) and its

measurement of force (inferiorly pointed red arrows). Licensed for adaptation and distribution from https://creativecommons.org/licenses/by/4.0/.

Housed inside the molded inserts are two key structural elements: a 3D-printed probe holder, which supports the ultrasound probe in a stable and repeatable position, and a molded bracket that anchors the load cells in a fixed alignment (Figure 2). To maintain proper foot positioning and minimize unwanted motion, the Ultrashoe also includes adjustable neoprene straps with padding to secure the foot firmly within the shoe. Overall, the moldable and modular design of the Ultrashoe allows for scaling to different shoe sizes and several shoe sizes are available for use.

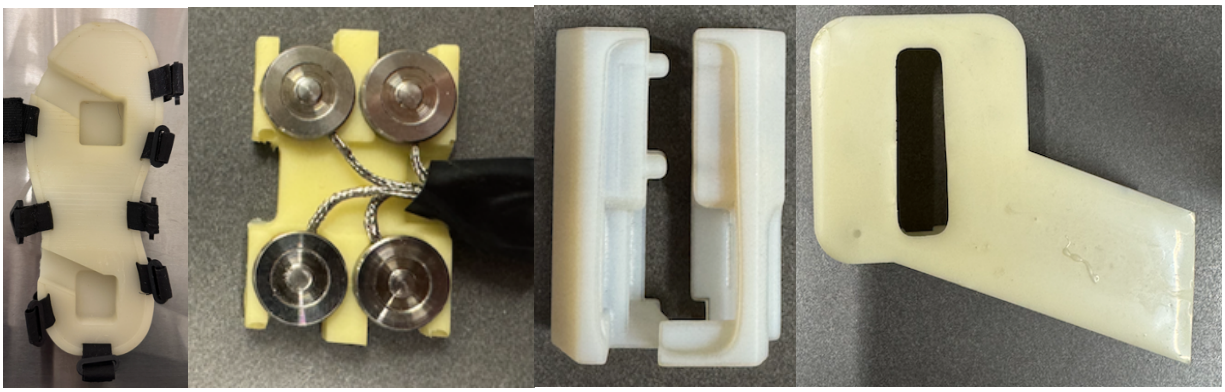

Figure 2: Ultrashoe components. The molded Ultrashoe sole (left), Honeywell Model 13 subminiature load cells on their molded housing (middle left), the 3D printed probe holder (middle right), and the heel housing that holds the components and fits into the Ultrashoe cavity. Not pictured: forefoot housing and ultrasound probe.

As a disclosure, the data collection of SA1 precedes my involvement with this project. A lab engineer at the Center for Limb Loss and MoBility (CLiMB) planned and executed this phase of the project. My involvement begins in the analysis portion of SA1 and continues for the entirety of the work in the rest of this thesis.

Ultrasound components

The ultrasound system of the Ultrashoe consists of a SuperSonic Imagine Aixplorer Multiwave scanner paired with a custom SLH20-6 “hockey stick” linear probe (Humanscan, Gyeonggi-Do, South Korea) (Figure 2). To accommodate the physical constraints of the Ultrashoe, the ultrasound probe was removed from its original housing, reducing its profile to fit within the shoe's structure. However, removing the casing exposes the internal wiring and compromises the structural integrity of the probe, increasing the risk of mechanical failure.

Figure 3: SuperSonic Imagine Aixplorer Multiwave scanner (left) and the custom ultrasound probe (right) SLH20-6 “hockey stick” linear probe (Humanscan, Gyeonggi-Do, South Korea).

To enable effective ultrasound transmission while avoiding the use of conventional gel, which is impractical due to the risk of contact with exposed electronics, Aquaflex ultrasound gel pads (Parker Labs, Fairfield, NJ) were used as a coupling medium. These pads were manually cut using a cheese cutter and box cutter to fit precisely over the probe’s contact area, ensuring consistent

acoustic coupling between the probe and the skin. Ultrasound image data is acquired directly on the Aixplorer system and subsequently exported to a USB drive for post-processing and analysis.

Data Acquisition

The second component of the Ultrashoe setup is the data acquisition hardware and software. All data except for the ultrasound collection was through a National Instruments (NI) cDAQ-9178 and LabVIEW code, interacting with the front panel (Figure 3). The Aixplorer is not set up for live data streaming or live syncing to the DAQ system.

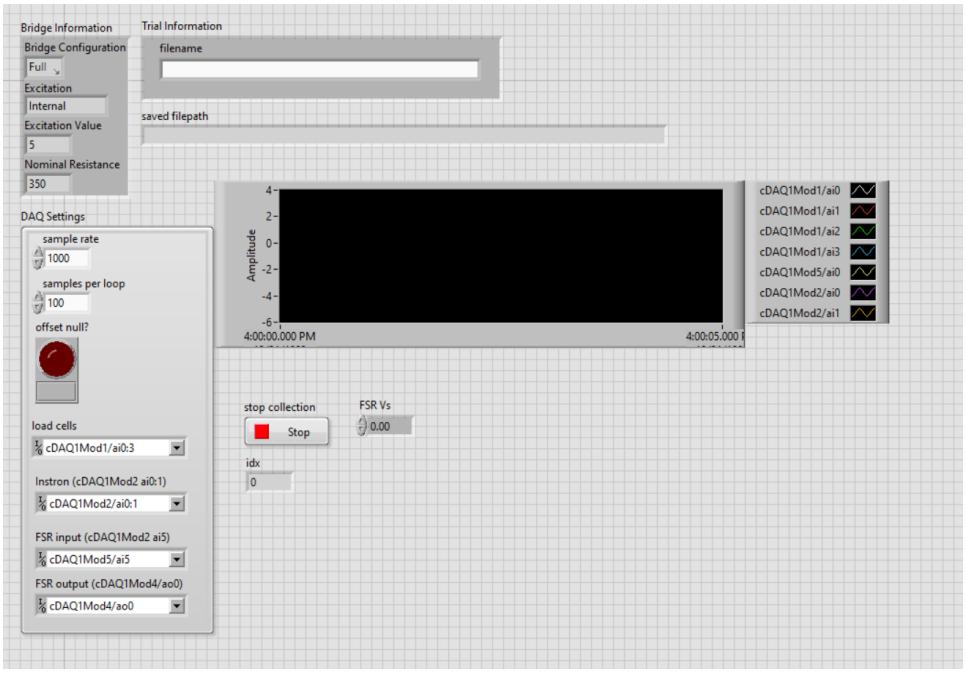

Figure 4: LabVIEW front panel for the data collection.

Force data was captured via four Honeywell Model 13 Subminiature Load Cells (Charlotte, NC) which are rated up to 250 lbs (Figure 2). They are small enough that four can fit in parallel on a small, molded holding platform that is in series with the ultrasound probe. The load cells being in parallel means that, together, they can tolerate loads much greater than 250 lbs if the loads are

relatively evenly distributed across the sensors. These are hooked up to an NI 9237 4-Ch 24-Bit Half/Full Bridge Analog Input module for recording the load cell data.

A second data stream is captured from an Instron E3000 materials testing machine, which outputs analog signals for both force and displacement. These signals are recorded as voltages using an NI 9205 32-channel, ±200 mV, 16-bit Analog Input module. Calibration and scaling are performed using a conversion factor specified within the Instron Console software.

To synchronize ultrasound data with the DAQ system, a force-sensitive resistor (FSR) was mounted over the acquisition button on the Aixplorer ultrasound system. A voltage signal is output via an NI 9263 4-channel, ± 10 V, 16-bit Analog Output module, routed through a voltage divider circuit and recorded by another NI 9205 module. Voltage is supplied to the voltage divider (5 V) such that when the FSR is pressed, the spike in the signal will be ~3 V. This synchronization pulse marks the moment of ultrasound image acquisition, allowing it to be aligned temporally with load cell and Instron data during post-processing.

The LabVIEW script used for data acquisition is a modified version of the example analog input program provided within the LabVIEW software environment. LabVIEW is a graphical programming language that operates on a dataflow paradigm, meaning it does not execute instructions in a top-down, line-by-line manner like traditional text-based languages. Instead, program execution is determined by the flow of data between function blocks. The LabVIEW environment is composed of two main components: the front panel, which serves as the graphical

user interface for interacting with the program during execution, and the block diagram, where the user defines the functional logic by placing and wiring together graphical nodes.

The script includes two data streams. The data output stream handles analog voltage output, which sends a constant user-defined voltage to the voltage divider circuit. This stream does not require synchronization with the analog input data, as it simply maintains a fixed output level throughout the trial. The data input stream is responsible for acquiring analog input signals from multiple sources, including the load cells, Instron output channels, and the FSR. These inputs are sampled using the same clock to ensure temporal alignment across all signals.

The program is initiated by user interaction and continues to acquire data until the “STOP” button is pressed. Pressing STOP terminates the while loop, ends acquisition, and triggers data saving routines to store the collected data for post-processing.

On the front panel, users can define key acquisition parameters, including the sampling rate, file save path, and custom names for each sensor channel. The panel also includes controls for configuring bridge settings for the load cells, such as excitation voltage and scaling parameters. A feature to perform offset nulling (which zeros the load cell readings at the beginning of the acquisition) is built into the panel. However, this function was disabled during testing, as the experimental protocol began with a non-zero preload force, making automatic zeroing inappropriate for those conditions.

(SA1) Identify ideal speeds of sound for plantar tissue

The first specific aim was to determine the ideal speed of sound (SoS) for accurate distance calculations from the collected ultrasound and CT data. Ultrasound systems assume a specific SoS to compute distances, but this value can vary across different tissue types. Because the heel pad and the tissue beneath the second metatarsal head contain a combination of skin, fat, muscle, tendon, and ligaments, this investigation aimed to identify the optimal SoS for precise ultrasound-based distance measurements. Accurate measurements are essential for improving the reliability of the derived mechanical properties.

Data collection

This investigation was executed by securing room temperature cadaveric feed (n=9) to the Ultrashoe and positioning it inside a LineUp cone-beam, weightbearing CT scanner (CurveBeam, voxel size: 0.3 × 0.3 × 0.3 mm, Hatfield, PA) (Figure 5). Ultrasound images and CT scans of various foot angles (to simulate heel strike and toe off) and amount of tibial loading (i.e., conditions=58) were captured at the heel or second metatarsal head. Imaging was performed in Pen/Med mode (6 MHz) with multiple assumed speeds of sound using the Aixplorer Multiwave's TissueTuner function, which allowed for selection of four discrete speeds of sound to use (1480, 1540, 1600, 1660 m/s). Using each speed of sound per CT scan, a total of 232 ultrasound scans were taken (58 conditions * 4 speeds of sound). However, samples TK 10 & TK 6 were dropped from subsequent analysis due to having abnormal errors that are assumed to be a result of experimental conditions, and 208 scans were processed. Of the cadavers used, the majority were Caucasian (8/9) and left feet (8/9) and male (7/9), and the average age was 63 years old (Table 2).

Figure 5: Experimental setup for collecting simultaneous ultrasound using and computed tomography scans inside a LineUp cone-beam, weightbearing CT scanner.

Sample	Age	Race	Sex	Side	BMI	# of scans
TK 1	77	C	M	L	26.57	13
TK 3	55	C	F	L	33.98	16
TK 6	73	C	M	R	24.85	3
TK 7	70	C	M	L	23.56	13
TK 8	73	C	M	L	24.85	3
TK 9	73	C	M	L	25.98	3
TK 10	53	C	F	L	24.71	3
UK 1	71	C	M	L	22.13	2
UK 2	29	AA	M	L	25.63	2

Table 2: For race, C indicates Caucasian and AA indicates Asian American. For sex, M indicates male, and F indicates female. Body mass index (BMI) was calculated using the formula: 703 × weight (lbs) / height (in)².

Ultrasound Analysis

Analysis of the ultrasound data involved several key steps: 1) preprocessing to enable batch processing of the data, 2) labeling of the ultrasound images using OpenCV, and 3) calculation of vertical distances for comparison with corresponding CT measurements.

Preprocessing data

To enable batch processing of the data, several preprocessing steps were taken. First, a Python Anaconda environment was created to support all required packages for this and subsequent analyses. Once the environment was established, all collected DICOM files were iterated through and saved as .jpg images in a new directory to facilitate easier handling. Additionally, pixel spacing values, used to convert pixel measurements to real-world distances, were extracted from each DICOM file and compiled into a single .csv file for easy reference.

Labeling data

The OpenCV package (i.e., open computer vision or cv2) was used to label the probe and bone surfaces in the ultrasound images. The labeling script iterates through all .jpg ultrasound images, opening one at a time in cv2, and allows the user to draw splines along the surfaces of interest of the bone and probe surfaces using the mouse (Figures 6 and 7). An undo function is included in case the user is not satisfied with a label. After labeling, the script saves a .txt file in a new directory, where each row contains the coordinates of a labeled pixel and the corresponding structure it belongs to (e.g., x=520, y=430, Bone). The script also checks for existing labels before

opening each file, eliminating the need to manually track which samples have already been processed.

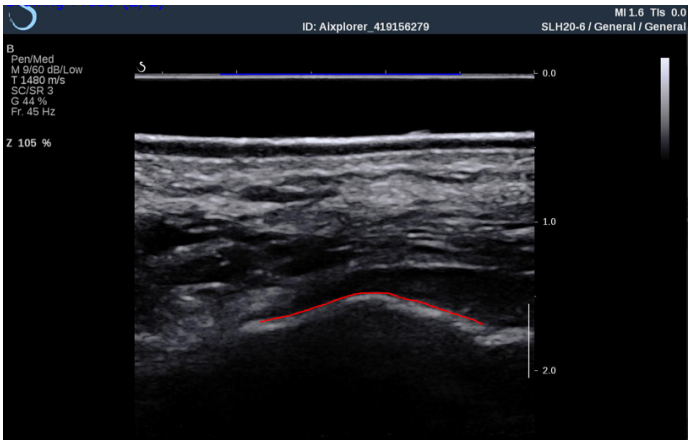

Figure 6: Labeled ultrasound image of the heel with the calcaneus (red) and probe (blue) labeled.

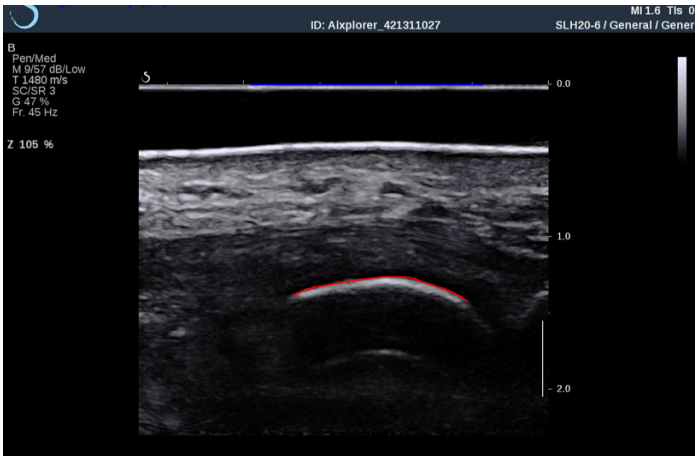

Figure 7: Labeled ultrasound image of the second metatarsal head (red) and probe (blue) labeled.

Calculating distances

To calculate the distances, the .txt label files were iterated through and matched with the corresponding pixel spacing values. For each .txt file, the y-distance from each bone point to the average probe y-value was computed. These distances were then overlaid on the ultrasound images to verify that the labels were accurate and that the resulting measurements were physiologically

plausible (Figure 8). Finally, the calculated vertical distances were compiled into a single .csv file for subsequent comparison with CT-derived distances.

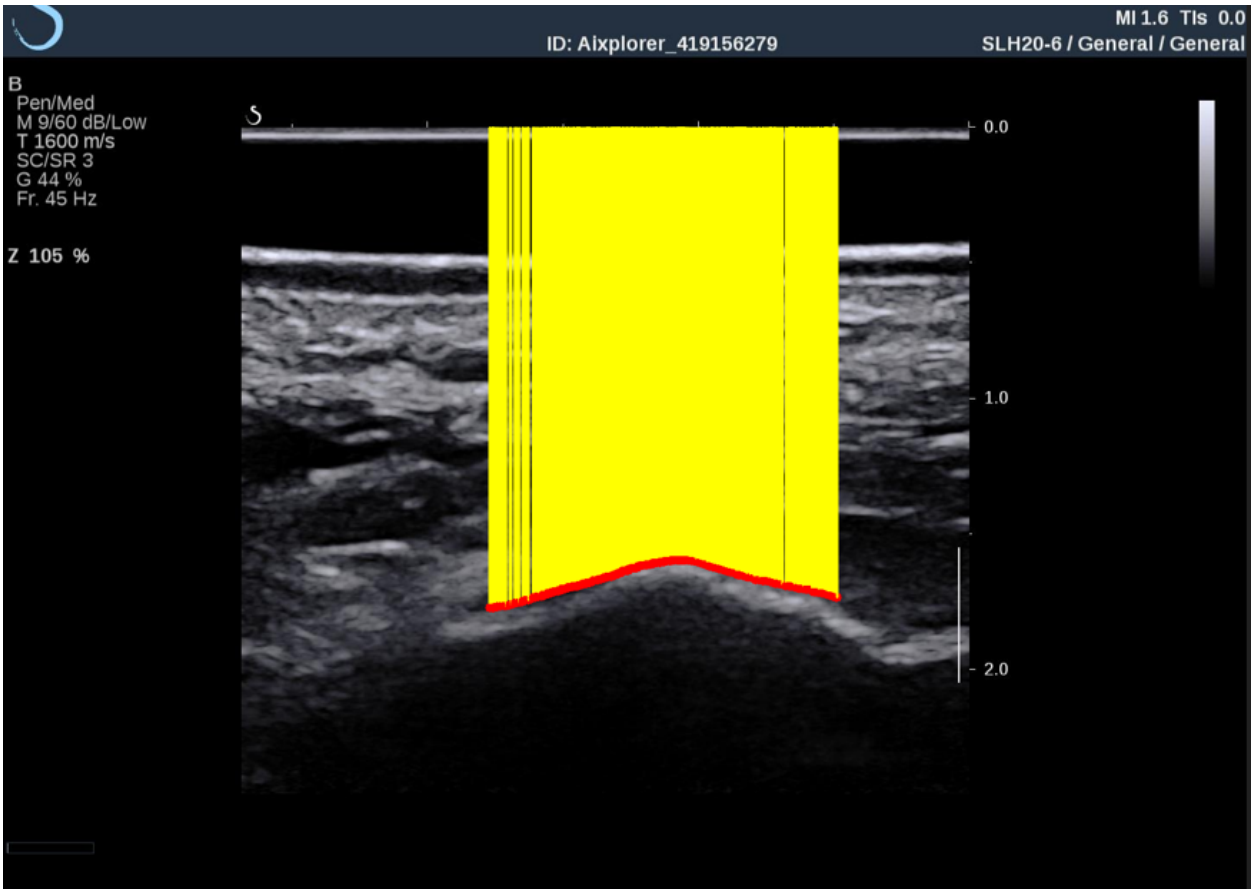

Figure 8: Vertical distances (yellow) overlaid over an ultrasound image of the heel with the calcaneus (red) and probe (blue) labeled.

CT data pipeline

CT scan segmentation

The first step in processing the CT scans was to segment the relevant bony structures. While CT provides excellent resolution for bone, it is less effective at distinguishing between soft tissues. Differentiating the skin from gel pad proved challenging, which was the reason for doing probe-

to-bone distance, rather than skin-to-bone. All initial CT processing was conducted in MIMICS [44] (Figures 9 and 10).

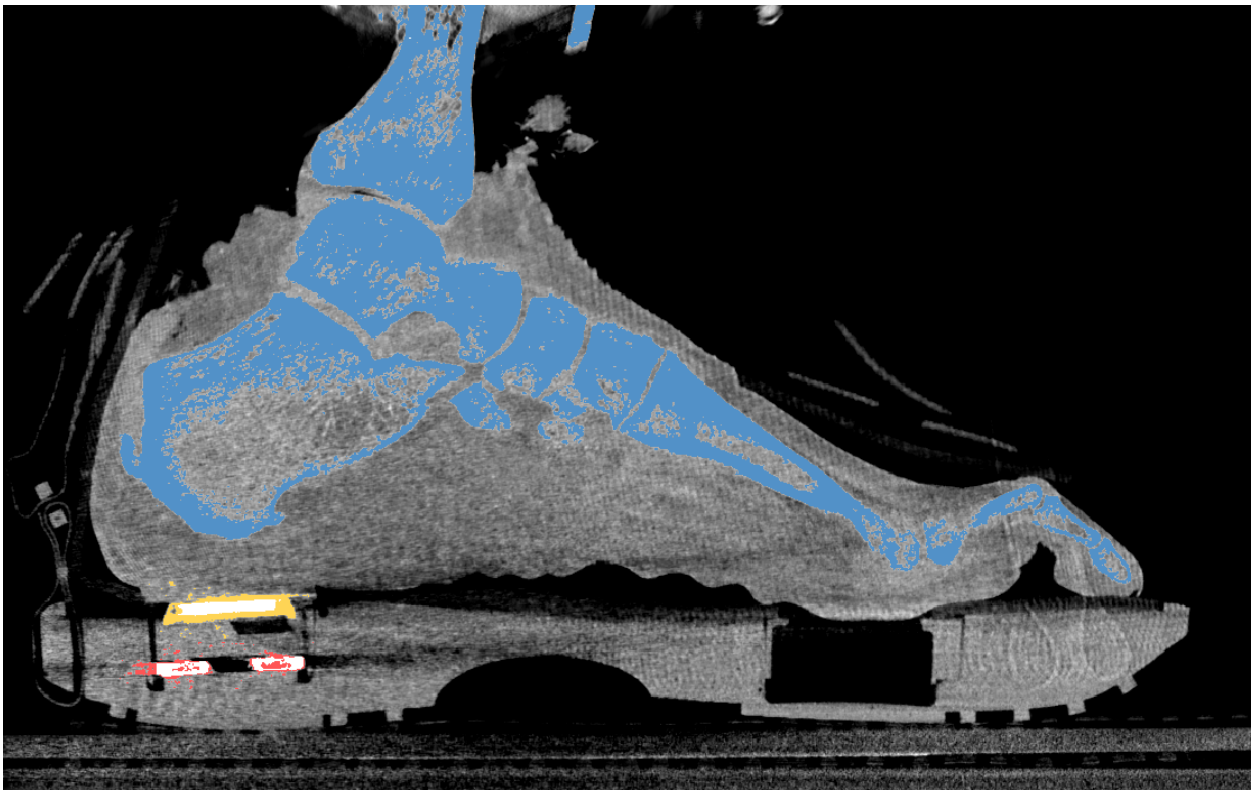

Figure 9: CT image of a cadaveric foot inside the Ultrashoe. The bones in the foot (blue), the ultrasound probe (yellow), and the load cells (red) are highlighted. The edge of the gel pad can be partially discerned at the lower left edge near the probe, but it is hard to distinguish from tissue in the area of contact with the probe.

Batch processing was done on the CT scans using identified Hounsfield unit (HU) thresholds, values that quantify X-ray attenuation in CT scans, to define the bounds for bone and probe materials (Figure 10). A script was written to create MIMICS files (.mcs) files from all the CT scans. The main automation script interacted with MIMICS with Python by iterating over all the .mcs project files, creating a bone and probe mask, then exporting these as .stl files.

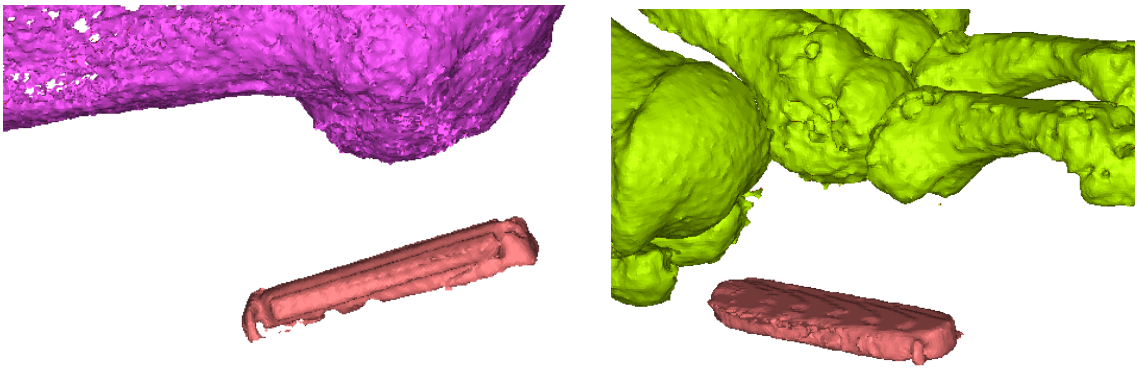

Figure 10: Processed computed tomography scans of the ultrasound probe (red), calcaneus (magenta), and metatarsals (lime green) inside MIMICS.

Segmentation was based on a range of HU for bone [350, 1988] and the probe [2222, 16882] based on manual testing to identify optimal values for the dataset. In Python, each CT project was iterated over, masks were created based on these thresholds, and corresponding .stl files were exported. Anecdotally, the method worked very well for the probe, moderately well for the calcaneus, and poorly for the second metatarsal head. Scans with acceptable segmentations were retained, while others exhibited issues such as extraneous mesh between the probe and bone or holes in the bone mesh. Unsatisfactory scans were reprocessed in MIMICS and, when necessary, further cleaned in MeshLab or MeshInspector on an ad hoc basis. The final masks and .stl meshes were qualitatively assessed to ensure that debris was not present between the probe and bone, surface smoothness was adequate, and the mesh was continuous in the region of interest.

CT labeling data

The labeling process involved two stages of user input: first, labeling the probe to calculate a projection plane, and second, labeling the bone at the intersection with this plane. The vedo [45] library in Python was used for this step due to its capabilities for 3D visualization and ability to calculate distances and geometries.

The first task was labeling the probe plane. Each probe mesh (.stl file) was loaded into Python and visualized using vedo (Figure 11). The user selected over 30 points on the top surface of the probe to provide a sufficient sample for fitting a plane using singular value decomposition (SVD). The first and last selected points were required to lie along the midline of the probe, as these were used to define the midline of the perpendicular plane that will extend to the bone. The code iterated through all probe mesh files and saved the selected points (x, y, z) into a .txt file.

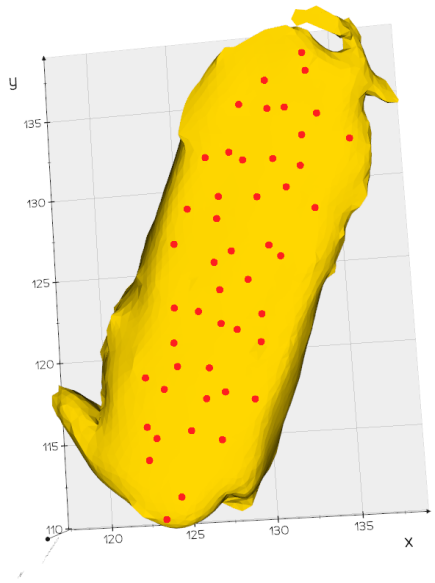

Figure 11: Example labeling of the probe plane. The superior surface of the probe was labeled with at least forty points with the first and last points being labeled along the estimated midline of the probe.

Using SVD, a plane was fit to the labeled probe points. A midline was then calculated from the first and last points in the probe point file. Together, the probe plane and midline were used to compute a perpendicular plane representing the direction of ultrasound wave propagation. This line was expected to intersect the bone and approximate the ultrasound imaging path. The probe plane should align with the probe surface, and the perpendicular line should intersect the bone at

a reasonable angle from the probe; both conditions were qualitatively verified during labeling. If either condition was unsatisfactory, the probe plane was relabeled, and mesh quality was reassessed.

Once confirmed, the user labeled sequential points along the bone surface where it intersected the perpendicular plane (Figure 12). Sequential labeling was required for the subsequent analysis code to function properly as a spline is fitted to the labeled points in the analyses. These bone points were saved in the same format as the probe points, with each file saved as a .txt.

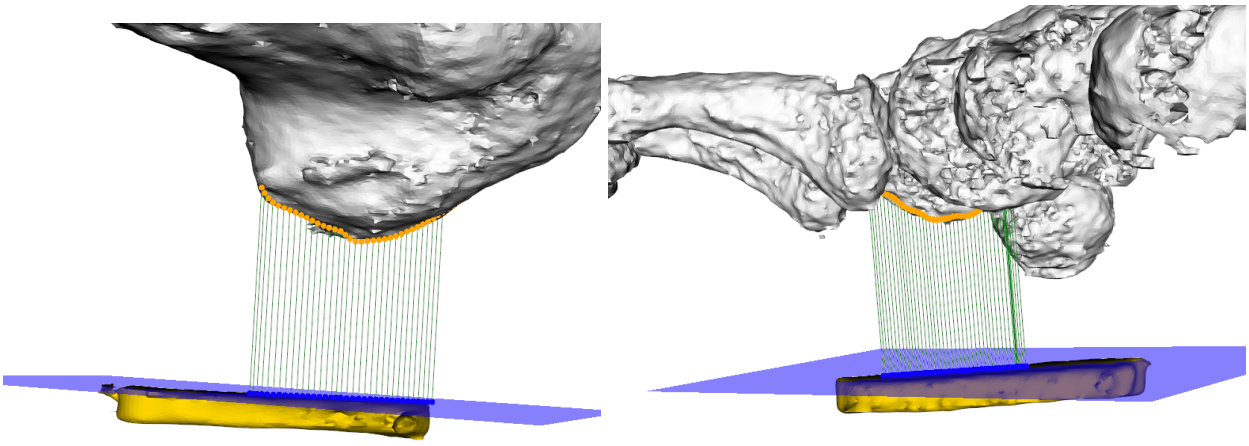

Figure 12: Example of the probe (yellow), fitted probe plane (blue), calculated distanced about the midline of the probe (green), and the individual points on the bone of interest (orange). The calcaneus (left) and second metatarsal head (right) are shown.

CT calculating distances

To calculate the distance between the probe and the bone, several steps were taken to ensure the measurement was aligned with the midline and followed the direction of the perpendicular projection plane. First, one hundred points were sampled along the midline of the probe. A spline (i.e., a piecewise polynomial function) was then fit to the labeled bone points and resampled to

one hundred points. These bone points were filtered to focus only on the region nearest to the probe. Both the midline and filtered bone points were then resampled to fifty points each for alignment. The bone points were subsequently projected onto the probe plane using:

$$3)\ \boldsymbol{p}_{proj} = \boldsymbol{p} - [(\boldsymbol{p} - \boldsymbol{c}) \cdot \boldsymbol{n}]\boldsymbol{n}$$

Where p is the sampled bone points, c is the centroid of the probe, and n is the unit plane normal vector. Then, distances are calculated from the bone points to the projected points onto the plane:

$$4)\ \boldsymbol{d} = |(\boldsymbol{p} - \boldsymbol{c}) \cdot \boldsymbol{n}|$$

The calculated distances are then validated to ensure they are aligned with the midline. After validation, the two meshes, the original bone points, the projected points on the probe plane, and the connecting distance lines are all plotted in vedo for qualitative confirmation. This code exists in two versions: the first allows the user to manually select a scan and does not save any calculations, serving as a validation tool to ensure the distances are computed correctly. The second version loops through all relevant scans, omits the visualization, and saves the calculated distances into a .csv file for later comparison with the ultrasound data.

Comparison between US and CT

This code executes the complete analysis of the ultrasound and CT-derived distances. It reads in the vertical distances from the ultrasound and the distances along the perpendicular plane from the CT scans. The first step involves cleaning the metadata from both datasets to ensure correct alignment for comparison. All distances from the ultrasound and CT data are then resampled to one hundred points. To directly compare the distances between modalities, the minimum distance between each set is evaluated. A threshold of 1.0% was applied to smooth out fluctuations in the

identified minimum values. Distances falling within this threshold were averaged and used for comparison. Both absolute distance differences and percent error were calculated, and all values were compiled into a summary .csv file. The remaining portion of the code generates plots to compare the data across different subjects, anatomical regions (heel vs. second metatarsal head), and assumed speeds of sound.

A note on automation in medical imaging

Several attempts were made to explore automation of the analysis pipeline. The first involved processing CT scans in MIMICS using its Python automation feature. While this approach succeeded for some scans, the majority required additional manual processing to be usable in subsequent analyses. A second attempt focused on identifying the outline of the bone of interest algorithmically. This area was of particular interest due to the substantial time required to label each ultrasound image. Given the volume of data to be collected (45 frames × 2 splines per frame × 60 seconds = 5400 splines per minute of data), automating this step could significantly improve efficiency in analysis. If the Ultrashoe is to be used more routinely in research, this avenue may warrant further exploration. For the current analysis, however, manual labeling was chosen.

(SA2) Load cell Instron validation

To validate the load cells after individual calibration, they were tested in the following three configurations: 1) the four load cells in parallel in the molded load cell holder component, 2) the four load cells in parallel in their housing with the ultrasound probe in series (but outside the Ultrashoe), and 3) four load cells in parallel in their housing with the ultrasound probe in series

inside the forefoot and heel in the Ultrashoe. The individual calibration was done to ensure that the readings matched the applied load from the Instron and if they did not then the calibration factor was adjusted to match the known applied load.

Load cell calibration

The load cells (Honeywell Model 13 Subminiature Load Cells) were measured using an NI 9237 analog input with a 5 V excitation voltage. The conversion from the measured values to the load in newtons is:

$$2)\ F_N = \frac{\boldsymbol{x}}{c} * \frac{V_{exc}}{V_{exc}} * 250\ lbs * 4.448 \frac{N}{lbs}$$

Where x is the measured signal in mV/V and c is the calibration factor in mV/V. For three of the four load cells there was a known calibration factor from the manufacturer that was recommended across the entire load range (i.e., 250 lbs). It had been several years since they were calibrated from the manufacturer, and all the load cells were adjusted slightly against the Instron to better match up with this reading.

The measurements from the Instron E3000 were taken by directly measuring the load and position directly from the load cell using analog output cables. The conversion factors used for force and position were 50 N/V and 3 mm/V, respectively. These were changeable inside the Instron Console software and the conversion factors selected were to maximize the resolution in the window of testing conducted and voltage limits of the DAQ boards.

Both load cell data and Instron data were collected using the custom LabVIEW protocol developed for this project and the raw recorded voltages were saved. All conversion factors and data augmentation were done post data collection.

For this testing, since we are aiming at validating the Ultrashoe at 250 N of peak force, we adjusted the calibration factor by manually adjusting until the peak load between the Instron and the load cells was minimized. The testing procedure for the individual load cell tuning was planned and executed using WaveMatrix to pre-load the sensors, offload to -1 N, a ramp to 200 N of compression, holding the force for two seconds, then a ramp back down to -1 N. A detailed description of the testing protocol is shown in the next section. The calibration factor was adjusted manually so that the peak load that was held was matched between the individual load cell and the readings from the Instron.

Load cell testing

In addition to calibrating the load cells, several different configurations were assessed to evaluate the accuracy of the load cells in the Ultrashoe. The first configuration included the load cells in parallel, mounted in their platform. The second configuration added the ultrasound probe and its holder, placed within the housing alongside the load cells and their platform. The third configuration included all housing components assembled within the Ultrashoe. The load cells in parallel were tested using a flat Instron compression platen, while the remaining configurations were tested using a custom fixture that applied load directly to the ultrasound probe (Figure 13).

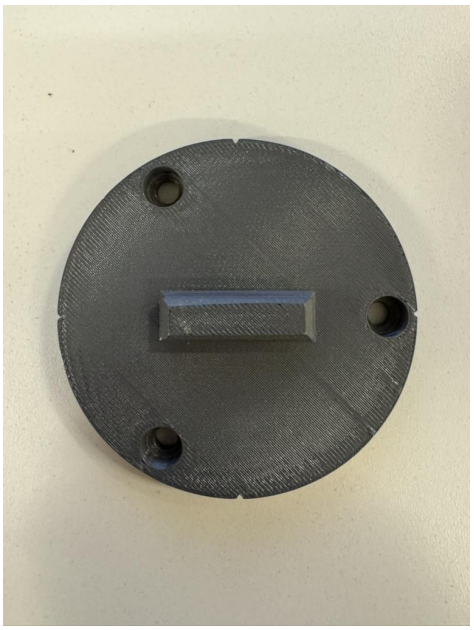

Figure 13: Platen attachment to Instron for applying load directly to the ultrasound probe.

The Instron can be used in either position or load control. Both were utilized to execute this testing, but load control was primarily used. The protocol for testing all three multi-load cell configurations was conducted as follows:

1. [Position control]: Move to a position of known contact with the material
2. *Start LabVIEW data collection*
3. [Load control]: Unload to -1 N
4. [Load control]: Hold for 2 s
5. [Load control]: Ramp to -200 N at 5 N/s
6. [Load control]: Hold for 2 s
7. [Load control]: Ramp to -1N at 5 N/s
8. [Load control]: Hold for 2 s

9. [Load control]: Triangle waveform of 200 N with 12 cycles at 0.5 Hz.
10. [Load control]: Hold for 2 s
11. Repeat 8-9 for frequencies of 1.0 Hz and 1.5 Hz.
12. [Position control]: Move to a position superior to the position at step 1.
13. * End LabVIEW data collection*

Analysis

The data were analyzed using custom Python scripts. Prior to conversion to force, filtering was done on the raw voltage signals using a fourth-order low-pass Butterworth filter with a cutoff frequency of 40 Hz (as to avoid over-smoothing of the triangle waves) and a sampling frequency of 1612.90 Hz. The portion of the testing procedure where the load was held at -1 N before the ramp loading was used to offset the Instron voltage reading (as there was a DC offset in the voltage readings from the Instron) and offset the combined load cell readings to -1 N. This area was detected by finding the gradient of the Instron force curve and identifying areas of no change (i.e., the place where the force was held at -1 N), and regions with consistent force rates (i.e., the ramp to -200 N). Reported measures start from where this plateau is identified and continue throughout the trial.

The next part of the analysis regarded applying a phase offset to the load cell data to match the Instron. Since the load cells are measuring the force through the ultrasound probe and a 3D printed probe holder piece there was a small delay in the measurement that ranged from 34-42 frames (~25 ms) to match the peaks. This was done using the function “correlate” from NumPy to find how

many indices the load cells need to be shifted to maximize the correlation between the curves and correcting the load cell combined data by this much. Then the difference between the curves was found starting at the plateau range of the first time it was held at -1 N.

(SA3) Ultrashoe Instron validation (cadaver foot)

The Ultrashoe was tested in series with a cadaveric foot and an Instron E3000 at the heel location. The cadaveric foot used was utilized in a previous study where a polyvinyl chloride (PVC) pipe with an outer diameter of 7.3 cm is potted to the tibia. A custom mount fit this PVC pipe to the Instron, and load was applied to the PVC pipe. Only the heel was assessed for this investigation as there will likely not be load transferred to the second metatarsal head in this experimental setup and it was deemed unphysiological to apply load directly to the second metatarsal head.

LabVIEW code

The same LabVIEW code used in SA2 was used for this testing procedure. The only difference is in the utilization of the FSR to synchronize the data from LabVIEW to the collected ultrasound data.

Experimental setup

The dynamic testing protocol proceeded in four main stages: system assembly and alignment, specimen preparation, experimental setup and calibration, and cyclic loading.

System Assembly and Alignment

The Ultrashoe device was first assembled by seating the ultrasound probe within its housing and arranging the four Honeywell button load cells in parallel inside their housing. After assembly, an ultrasound gel pad was applied directly to the probe face to guarantee consistent acoustic coupling with the cadaveric foot.

Instron - KUKA adapter

A 3D printed adapter was designed in SOLIDWORKS and printed with a Bambu 3D printer in polyethylene terephthalate glycol (PETG) for holding the PVC pipe in place during testing (Figure 14). The primary features are a wall to firmly hold the PVC pipe and a counterbored hole to mount to the Instron load cell.

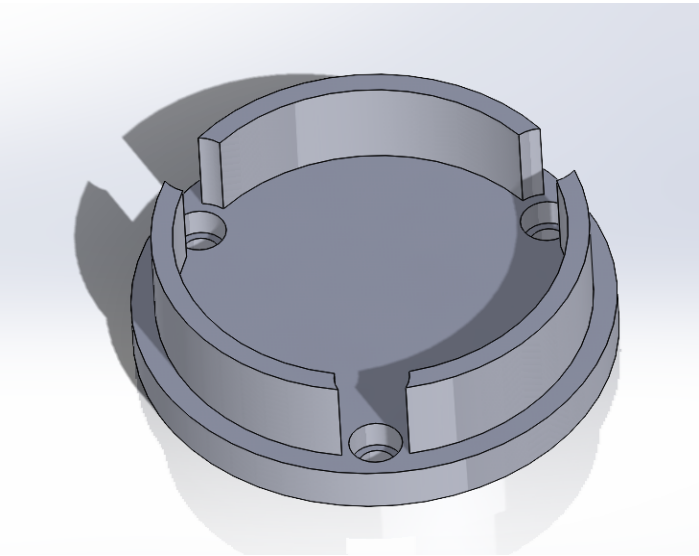

Figure 14: Instron-PVC adapter view in Solidworks.

Specimen Preparation

A frozen cadaveric foot that had been used previously was utilized for this investigation. Approximately 48 hours before testing, the foot was removed from the freezer and allowed to thaw. The specimen was brought to room temperature (approximately 75 °F) over the course of three hours prior to testing. The tibia was rigidly potted into a 7.3 cm–diameter PVC pipe for its previous study.

Experimental Setup and Calibration

The Instron-PVC adapter was secured to the upper crosshead of the Instron E3000 frame, and the PVC part of the cadaveric foot was fit inside the Instron-PVC adapter (Figure 15). The data-acquisition (DAQ) system was powered on, and each channel (four load cells, analog signals from the Instron, and the FSR) was verified that it was working properly. The Aixplorer ultrasound machine was powered up and configured to use the probe inside the Ultrashoe and ResMode was used to maximize resolution for imaging. The foot was manually translated mediolaterally and anteroposteriorly until a clear image of the calcaneus was on display.

Next, the Instron was tared to eliminate the weight of the PVC mount and using the Instron Tuning Wizard, a preliminary load of ~250 N was applied and held for ten seconds to tune the software's control scheme by estimating the stiffness of the material.

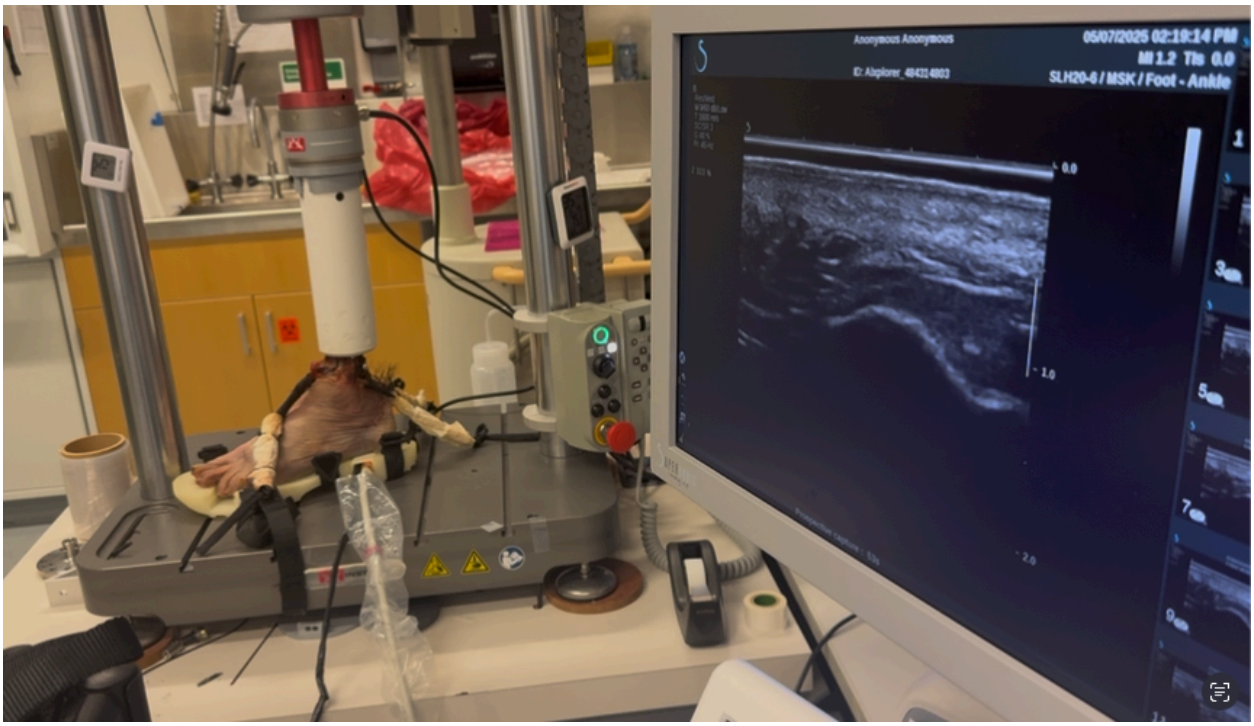

Figure 15: Testing setup for cadaveric testing inside the Instron E3000. Not pictured: data acquisition laptop and the Instron computer running WaveMatrix to execute the testing protocol.

Cyclic Loading Protocol

For each trial, one hundred preconditioning triangle waves were performed by ramping load from 0 to 200 N and back to 0 N at 1.0 Hz. The system was then paused for five seconds to account for the slight delay between pressing the button to save an ultrasound clip and when it starts recording. The main testing protocol consisted of twelve triangular load cycles from 0 to 200 N at three different frequencies (0.5 Hz, 1.0 Hz, and 1.5 Hz) was then conducted. Twelve cycles were chosen so that the first and last cycles could be discarded in post-processing, thereby mitigating variability associated with the Instron's initial zero crossing and ramp down to zero load. Throughout each test, force and displacement were sampled at 1612.90 Hz, while ultrasound frames were captured at 45 Hz using speeds of sound of 1540 m/s and 1600 m/s. The reasoning for sampling at 1612.90

Hz is explained in the discussion section. All raw data streams were stored for offline synchronization, image segmentation, and stiffness calculation.

WaveMatrix testing procedure

The protocol for testing was conducted as followed:

1. [Position control]: Move to a position of known contact with the material
2. *Start LabVIEW data collection*
3. [Load control]: Triangle waveform of 200N with 50 cycles at 1.0 Hz.
4. [Load control]: Hold at -1 N for 2 s
    a. *Start ultrasound data collection, pressing on the FSR resistor to start ultrasound recording*
5. [Load control]: Triangle waveform of 200N with 12 cycles at 1.0 Hz.
6. [Load control]: Hold for 2s
    a. *End ultrasound data collection, pressing on the FSR resistor to end ultrasound recording*
7. [Position control]: Move to a position superior to the position at step 1.
8. * End LabVIEW data collection*

Analysis

The processing pipeline begins by converting multi-frame DICOM ultrasound files into individual JPEG images. Each DICOM file was read from a designated directory, its pixel data extracted, normalized, and saved frame-by-frame as JPEGs in uniquely named subfolders. Once the frames were extracted, an interactive labeling tool was used to annotate grayscale ultrasound images. The user selected a trial and manually traced specific structures, such as bone or probe, with optional enhancements like contrast-limited adaptive histogram equalization (CLAHE) and gamma correction to improve image clarity (Figure 16). Labeled splines were saved to text files for subsequent calculation of the distances.

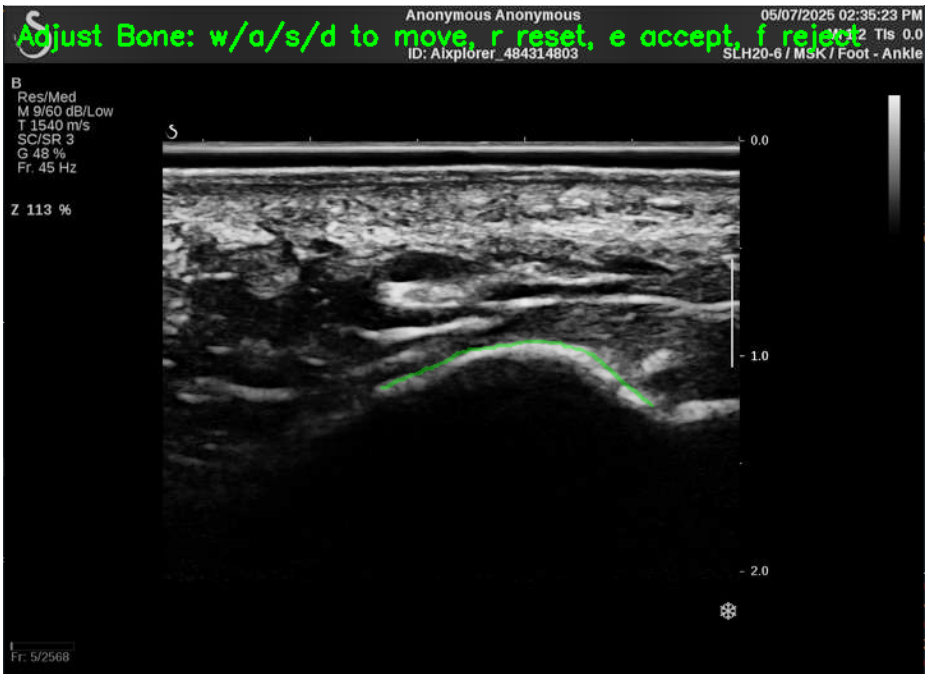

Figure 16: Labeling of the calcaneus surface.

With the labeled pixel coordinates, vertical distances between the bone and probe splines were calculated to estimate soft tissue thickness. These distances were matched by x-coordinate and converted to millimeters using trial-specific pixel spacing data taken from the DICOM files. Both

raw and condensed distance metrics were saved, the latter summarizing each frame by averaging values within 1% of the minimum distance. These distances were then synced with the load cell data from the DAQ system using the spike of the FSR signal for the start and end of the signal. The force data was interpolated to 1350 Hz (i.e., a multiple of 45 Hz), and both datasets were aligned by time using nearest-neighbor matching to create a unified dataset.

Aligned force and distance signals were then analyzed to quantify tissue stiffness. Peaks and troughs in both signals were identified on the raw signal (Figure 17), and stiffness was estimated as the slope between matched peak-to-trough points using the raw force curve and the smoothed distance curve. The filtering was done using a fourth-order low-pass Butterworth filter with a cutoff frequency of 5Hz. Stiffness was calculated in two ways: calculating the difference between the peak and trough of the force-deformation curve (Figure 18), and by fitting a linear curve to the final 50% of the force-deformation curve. Cycles were grouped by frequency (0.5 Hz, 1.0 Hz, and 1.5 Hz), and both fit-based and peak-to-trough stiffness metrics were calculated. Summary plots were generated for each cycle, and stiffness values were organized by frequency group.

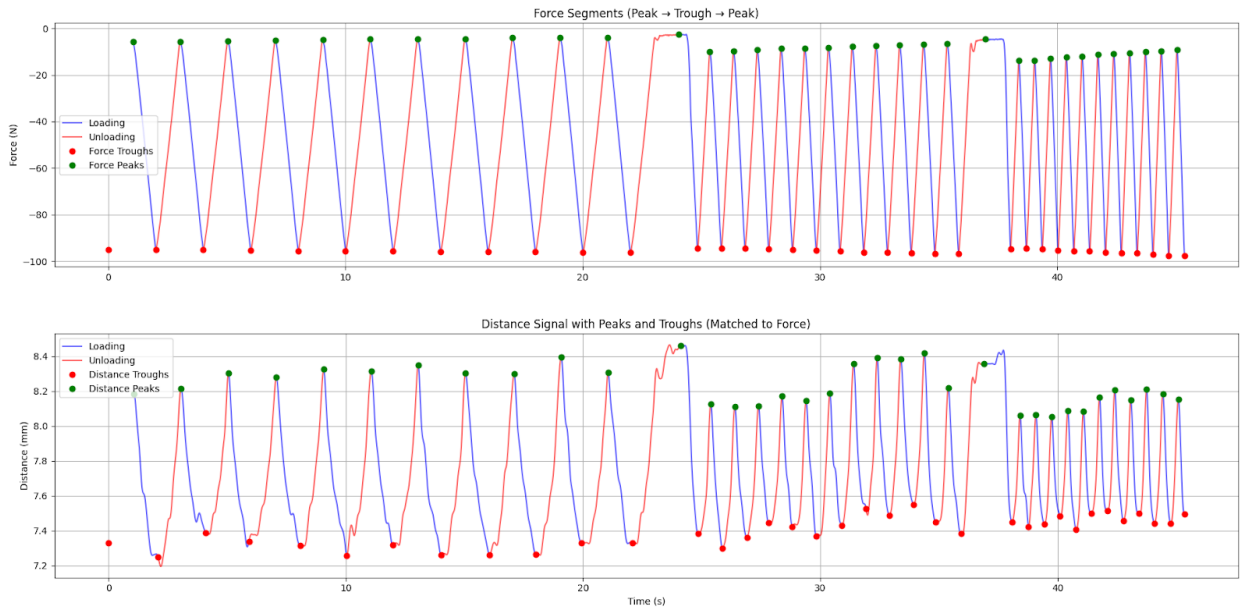

Figure 17: Identification of peaks (green dot), troughs (red dot), loading regions (blue curve), and unloading regions (red curve) for a sample trial.

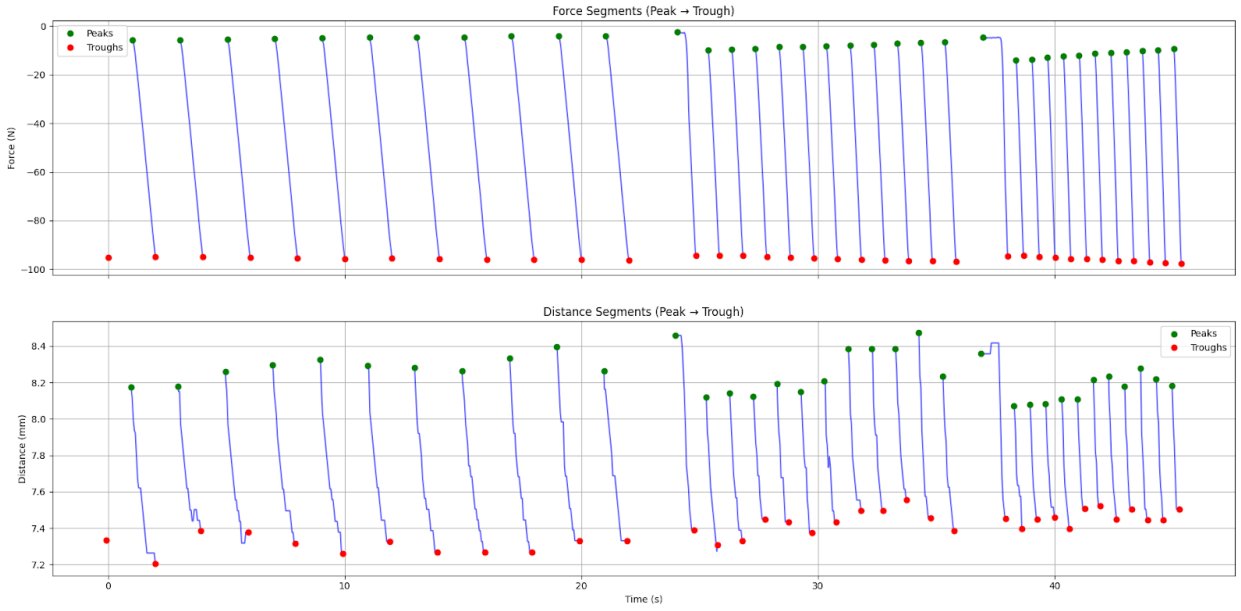

Figure 18: Segmentation of loading curves for subsequent stiffness calculation.

The final stage visualizes stiffness trends across trials and frequencies. A summary CSV was loaded and cleaned, then multiple boxplots were generated to compare stiffness across frequencies and between calculation methods. Results are shown both by individual trial groupings and pooled

across all trials. A combined plot allows direct comparison of fit-based versus peak-to-trough stiffness, providing a comprehensive view of the reliability, variability, and frequency dependence of the measurements.

Results

SA1 Results

Assumed speed of sound influences ultrasound distance accuracy, and it was shown that the commonly used speed of sound in soft tissue (1540 m/s) consistently underestimated the true distance. In contrast, 1600 m/s and 1660 m/s yielded more accurate results depending on anatomical location. In the heel, 1600 m/s produced the lowest error, while at the second metatarsal head, 1660 m/s resulted in the smallest mean absolute error, though the difference from 1600 m/s was minimal (Figures 19 and 20). Across both sites for different samples, 1600 m/s slightly underestimated and 1660 m/s slightly overestimated CT-derived distances. However, there was some variation between feet as to the ideal speed of sound (Figures 21 and 22). Sample “UK 1” had an ideal speed of sound for the heel at around 1480 m/s, however for the second metatarsal all used speeds of sound underestimated distance, implying a speed of sound greater than 1660 m/s was more accurate. Overall, most samples followed the trend of 1600 m/s slightly underestimating and 1660 m/s slightly distance, between both the heel and second metatarsal.

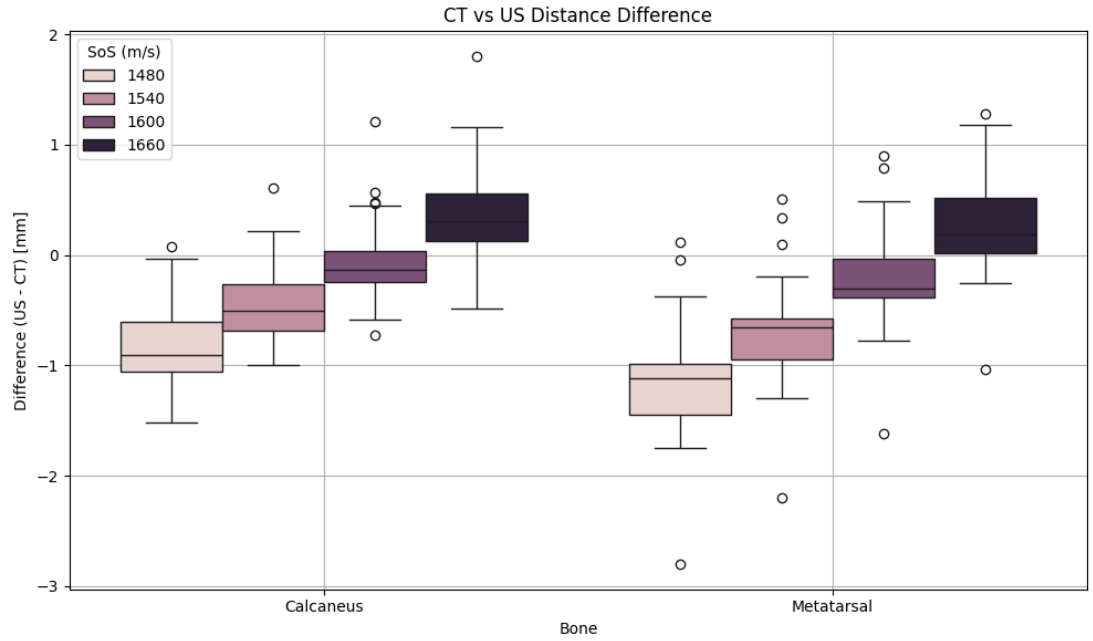

Figure 19: Comparison of the difference between the ultrasound-derived distances across different speeds of sound against the CT-derived distance

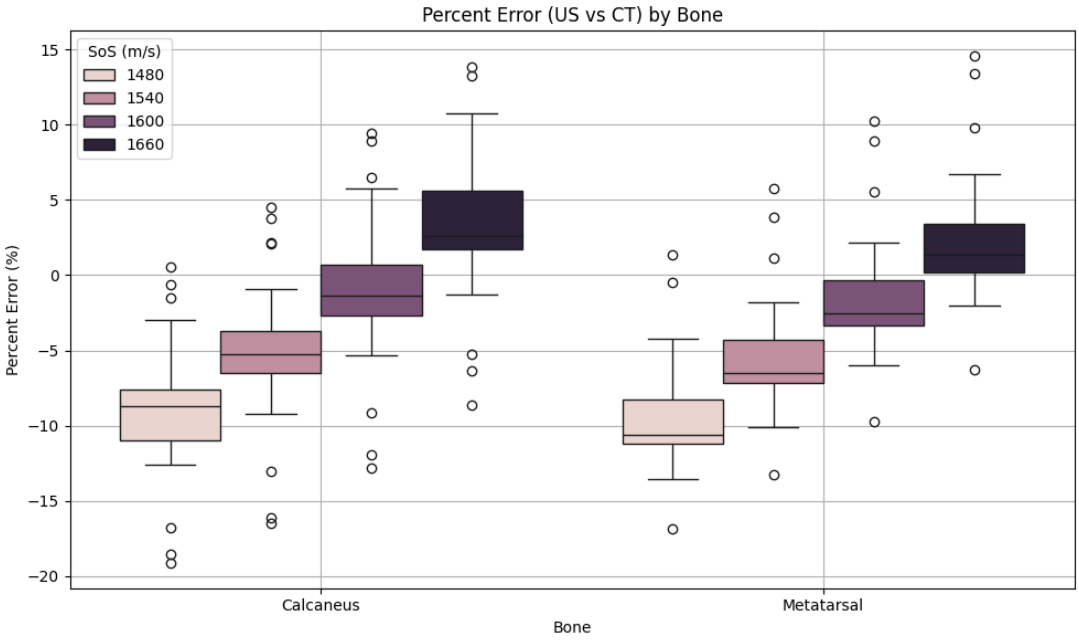

Figure 20: Comparison of the percentage error between the ultrasound-derived distances across different speeds of sound against the CT-derived distance.

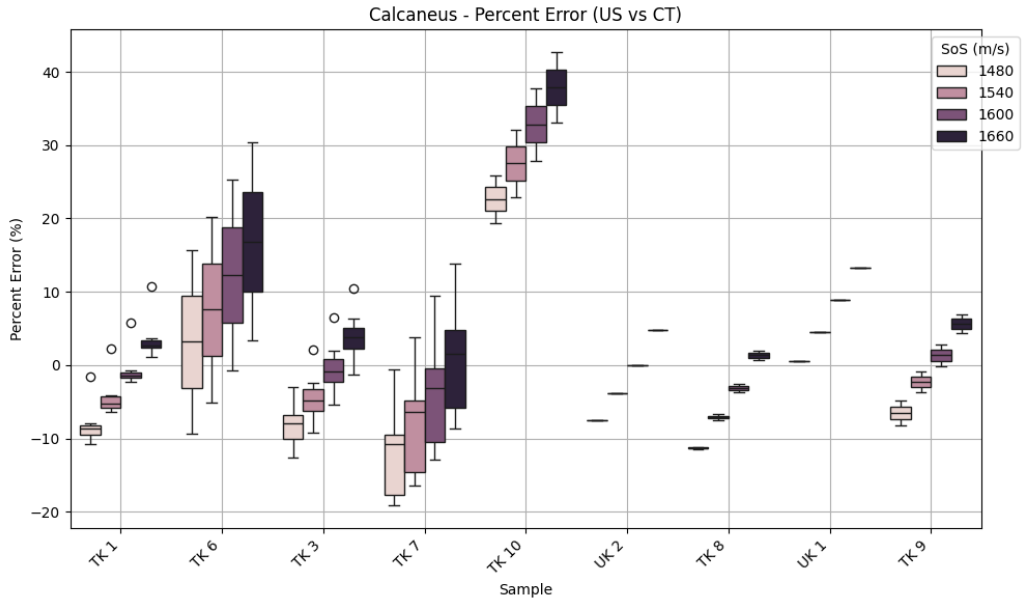

Figure 21: Comparison of the percentage errors across different cadaveric foot samples for the calcaneus.

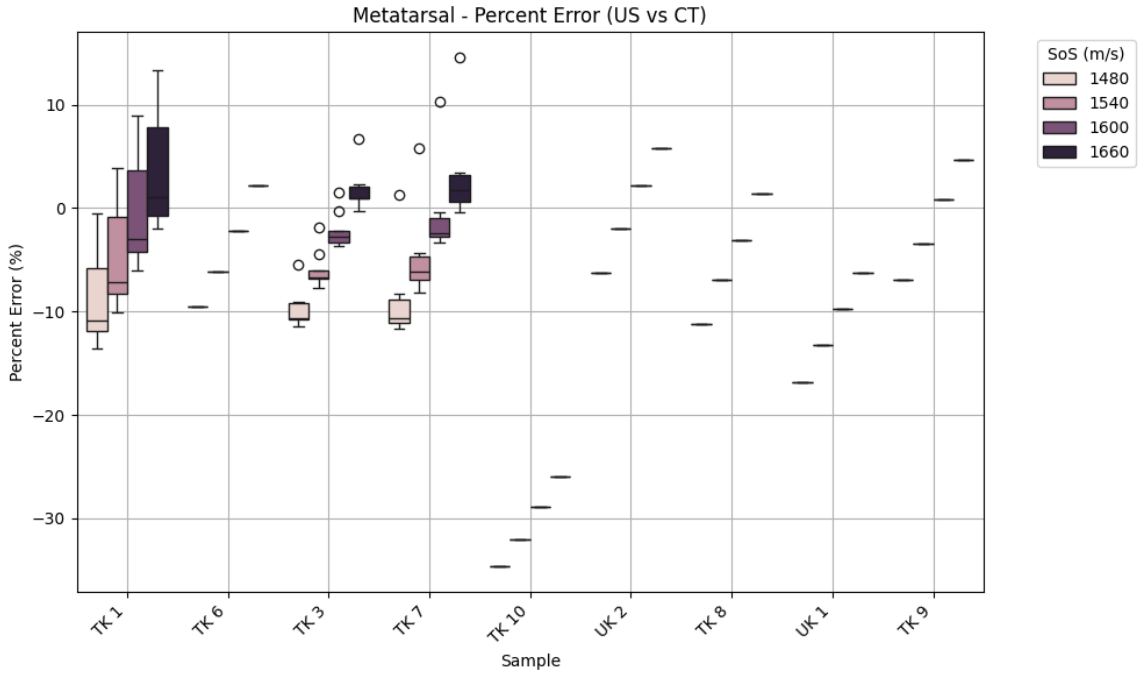

Figure 22: Comparison of the percentage errors across different cadaveric foot samples for the second metatarsal head.

Mean absolute error and mean signed error revealed both the optimal speed of sound for each anatomical site and the systematic bias introduced by different assumptions. The mean absolute error and mean signed error for each combination of anatomical location and speed of sound

assumption were summarized (Table 3). These results showed that 1600 m/s produced the lowest mean absolute error at the calcaneus, while 1660 m/s was most accurate at the metatarsal head. Meanwhile, the mean signed error highlighted a consistent directional bias: 1600 m/s slightly underestimated and 1660 m/s slightly overestimated the true distances.

SoS (m/s)	**Bone**	**Mean Absolute Error (mm)**	**Mean Signed Error (mm)**
1480	Calcaneus	0.824	-0.818
1540	Calcaneus	0.526	-0.441
1600	Calcaneus	0.312	-0.061
1660	Calcaneus	0.460	0.368
1480	Metatarsal	1.146	-1.136
1540	Metatarsal	0.742	-0.666
1600	Metatarsal	0.418	-0.187
1660	Metatarsal	0.391	0.271

Table 3: Mean Absolute and Signed Error by Bone and SoS

SA2 Results

The load cells exhibited low error overall, with accuracy decreasing as they were integrated into progressively more complex assemblies. The mean ± standard deviation of the absolute error was 1.774 ± 1.044 N in the parallel configuration, 2.030 ± 1.373 N when placed in the Ultrashoe

housing, and 3.787 ± 3.091 N in the fully assembled Ultrashoe. The errors were different when compared between the forefoot and the heel housing or location (Figure 23).

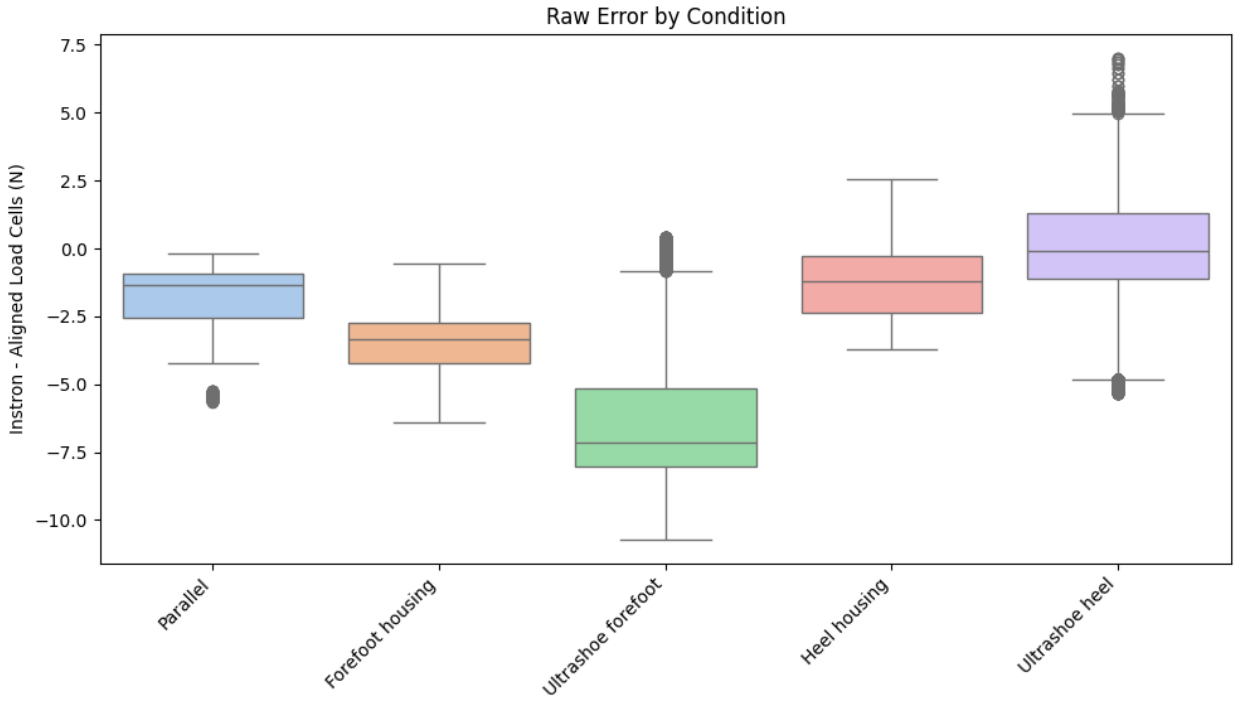

Figure 23: Boxplot of the error of the load cells in the different configurations including the load cells in parallel, the load cells in the heel or forefoot housing, and the Ultrashoe fully assembled in the forefoot or heel.

While the general shape of the force-deformation profile remained consistent across all setups, the Ultrashoe configuration exhibited slightly higher variability and higher peak errors compared to the simpler setups. These differences highlight the influence of the load path complexity on the fidelity of force measurements within the Ultrashoe system.

This work also served to evaluate the delay in the force transmission pathway from the ultrasound probe to the load cells. In the representative sample analyzed, a phase correction of 42 samples was required to align the force curves, which corresponds to approximately a 25 ms delay at a sampling rate of 1612.90 samples per second (Figure 24). This delay reflects the time difference

between when force is applied to the probe and when it is registered by the load cells. This finding will be considered when interpreting the results of SA3 with the cadaveric feet. A slight delay between the peaks of displacement and force is expected when using the Ultrashoe sensors, and the delay identified in SA2 will be used as a correction factor in SA3 if such peak offsets are observed.

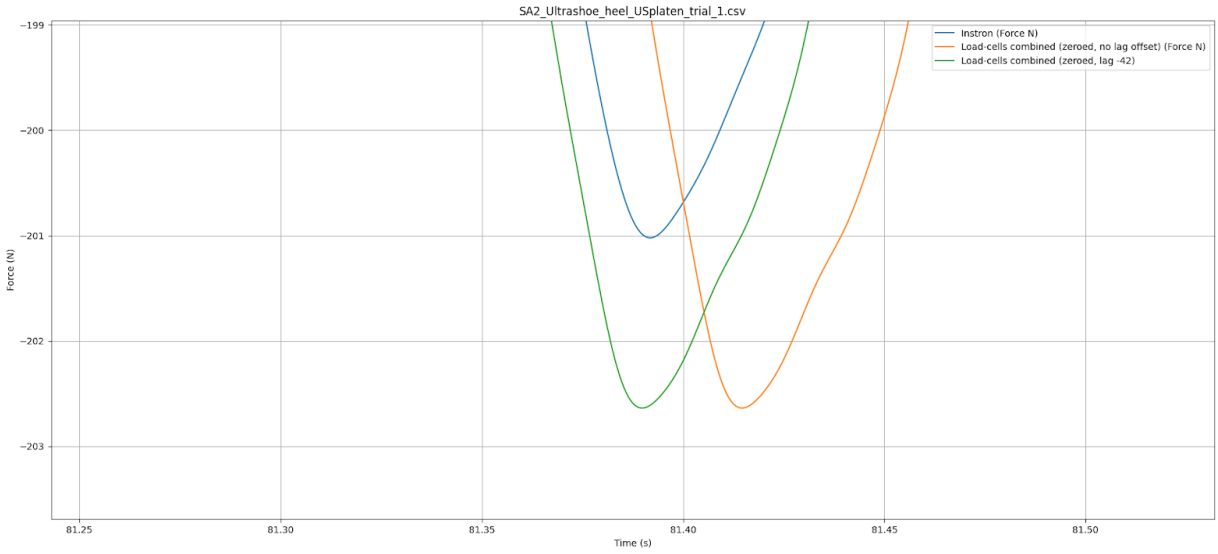

Figure 24: Phase correction of the load cell readings to the Instron force readings. The load cell readings (orange) were shifted (green) to match the Instron readings (blue).

SA3 Results

Calculated stiffness tended to increase with loading frequency and decrease with higher assumed speed of sound, indicating that both dynamic loading conditions and ultrasound reconstruction parameters influence mechanical property estimates. This trend was consistent for both peak-to-trough stiffness and fit stiffness. This demonstrates that the Ultrashoe captures frequency-dependent mechanical behavior of the plantar tissue and that assuming a higher speed of sound

consistently results in lower estimated stiffness values, due to spatial scaling effects in ultrasound image reconstruction (Table 4).

Speed of sound (m/s)	**Frequency (Hz)**	**Number of samples used (out of 30)**	**Fit Stiffness (N/mm)**	**Peak-to-trough stiffness (N/mm)**
1540	0.5	29	175.6 ± 50.53	92.16 ± 11.04
1540	1.0	29	193.97 ± 26.15	121.64 ± 11.28
1540	1.5	29	199.25 ± 24.39	139.27 ± 11.83
1600	0.5	28	139.33 ± 19.21	87.02 ± 5.11
1600	1.0	30	143.11 ± 21.95	103.99 ± 9.17
1600	1.5	30	170.68 ± 23.01	127.67 ± 12.1

Table 4: Results from stiffness calculations, with outliers dropped from analysis.

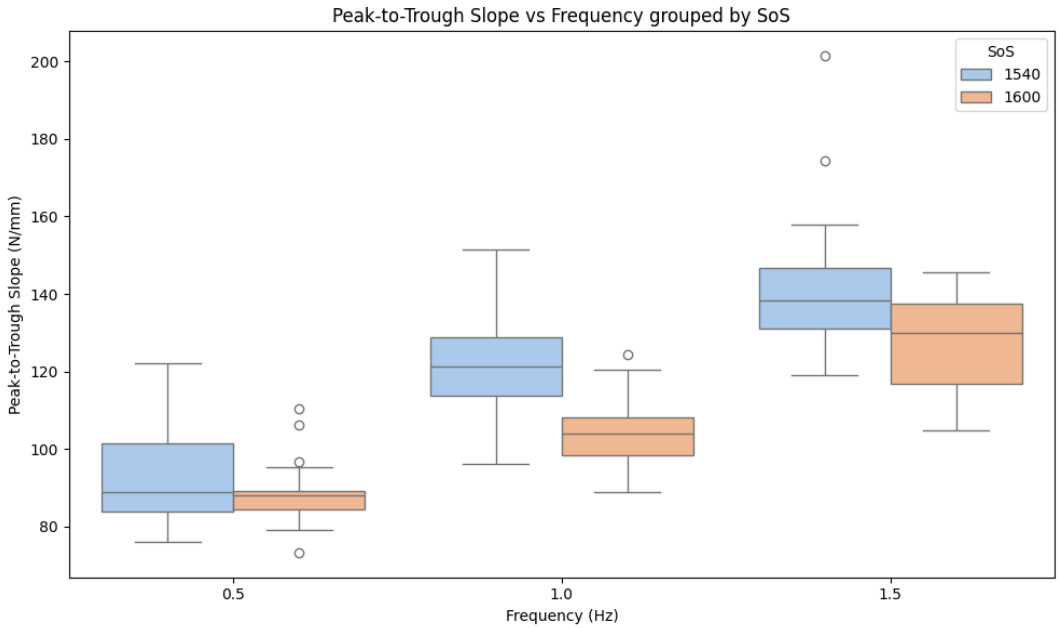

Figure 25: Comparison of calculated peak-to-trough stiffness (using the unloaded to loaded points) for ultrasound imaging of 1540 m/s and 1600 m/s across the three tested frequencies (0.5 Hz, 1.0 Hz, 1.5 Hz).

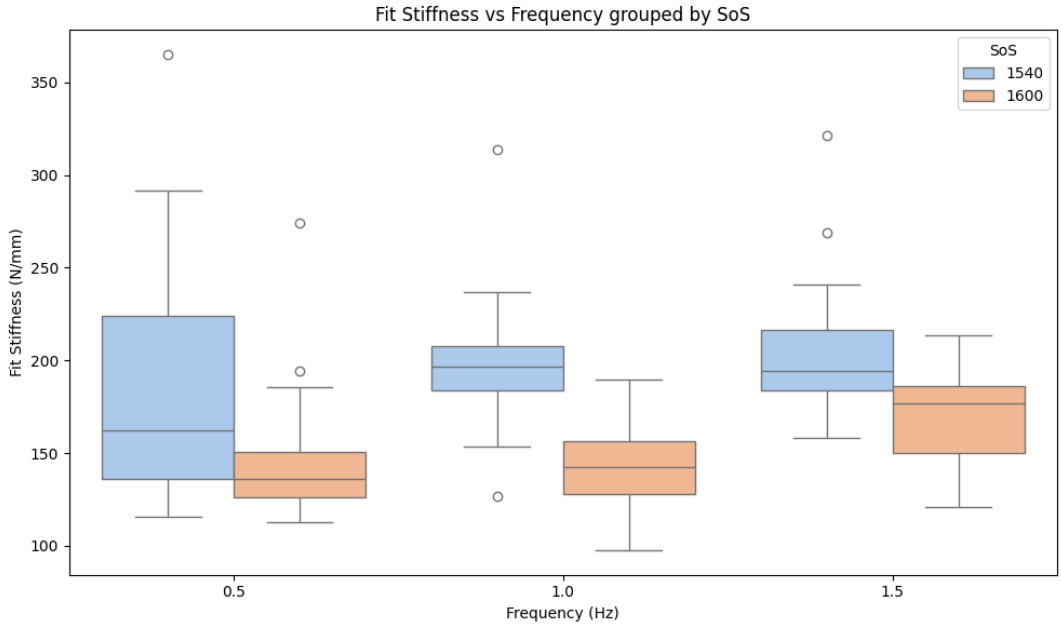

Figure 26: Comparison of calculated linear fit stiffness (using the last 50% of the loading curve) for ultrasound imaging of 1540 m/s and 1600 m/s across the three tested frequencies (0.5 Hz, 1.0 Hz, 1.5 Hz).

Discussion

This investigation focused on reducing uncertainty in measurements from the Ultrashoe sensors (SA1 and SA2) and demonstrating the device's capability to calculate plantar soft tissue stiffness in a controlled setting (SA3). The first objective was to identify the optimal speed of sound for imaging the heel and second metatarsal head, the two regions accessible to the Ultrashoe. Precise distance measurements are critical for accurate stiffness estimation. To address this, a novel method was used in which near-simultaneous CT and ultrasound images were collected across a range of assumed speeds of sound. This allowed for determining the speed that yielded the smallest error compared to CT-based distances.

The optimal speed of sound for the heel was 1600 m/s. For the second metatarsal head, both 1600 m/s and 1660 m/s produced similar results, with 1600 m/s tending to slightly underestimate and 1660 m/s slightly overestimate distances. This suggests that the true, aggregate speed of sound may lie between these two values. Due to the high composition of fat in the plantar soft tissue, specifically the heel, it was surprising that the optimal speed of sound was found to be so high. Several factors that may have caused this were the stiffness of the skin, the elastic septa in the fat pad lending more structural and mechanical integrity than other areas of fat in the body (e.g., in the abdomen), and that the cadaveric feet were at room temperature (~70 °F), rather than body temperature (98.2 °F) [46]. The role of temperature may have had an effect as at higher temperatures, we would expect fat to be more liquid and less stiff compared to lower temperatures.

It is important to note that individual variability in tissue composition may causes inter-subject differences in actual speed of sound. Additionally, structural changes that occur due to aging or diabetes may influence the speed that sound travels through the plantar soft tissue. Nonetheless, the goal of this study was to reduce measurement error within the constraints of the experimental setup. Compared to the standard clinical assumption of 1540 m/s, using 1600 m/s resulted in more accurate distance calculations.

A limitation of this work was that the ultrasound system only allowed selection of a few discrete speeds of sound (1480, 1540, 1600, and 1660 m/s). The ability to adjust in finer increments would have enabled a more precise evaluation. While the primary objective was to determine an appropriate speed of sound for plantar tissue, a secondary goal was to apply this value within the Ultrashoe to improve stiffness calculations. Although identifying an exact speed of sound may have limited clinical relevance due to the constraints of typical ultrasound machines, it would have a practical significance for the Ultrashoe and other research endeavors into the plantar soft tissue using ultrasound. Finally, the use of cadaveric feet represents another limitation. Although the simultaneous CT and ultrasound methodology could be applied in vivo, cadaveric specimens were selected to ensure greater control over experimental conditions and for ease of access. Additionally, the CT imaging was treated as ground-truth data, when in reality there is likely some degree of error associated with the data collection and processing of the bone and probe meshes. One report showed that the cone-beam scanner used for this study had root mean squared (RMS) errors of 0.43 ± 0.10 mm for the calcaneus compared to laser scanning of individual bones [47]. However, it was also demonstrated that the results (for the calcaneus) were highly consistent with an intraclass correlation coefficient of 0.992 ± 0.003. It is unknown if the CT scans used in SA1

were completely accurate, or if they were systematically underestimating or overestimating the size of the bones.

Probe-to-bone distances measured from CT were used instead of skin-to-bone distances. This choice was deemed necessary because the ultrasound probe was clearly visible on CT, whereas the skin surface was poorly defined due to contact with the Ultrashoe. One potential source of error was the calculation of the distance in the CT scans. This was an involved process that required user input and relied on the assumption that the path of the ultrasound image followed the midline of the ultrasound probe and started from the face visible on the probe face identifiable using the HU thresholding. The factors of variability associated with this methodology included the segmentation of the CT scans and the cleaning of scans, the points labeled on the probe and the subsequent fitting of the midline and plane using the SVD, and the labeling of points on the bone. A reliability study was not done to assess the consistency of this methodology.

The use of an ultrasound gel pad likely introduced additional error, as its speed of sound is expected to be lower than that of tissue, potentially biasing the results toward a lower optimal speed of sound. Unfortunately, the manufacturer does not report the exact speed of sound of the gel pad, and literature was not found to document a value, though it is assumed to be close to 1540 m/s. This is an interesting consideration, as it would imply that the speed of sound of just the tissue in the foot would skew slightly higher reported in this study since the overall speed of sound included the gel inside the distance calculation. In some scans, the amount of gel padding was minimal and in others that had the foot tilted to simulate heel strike or toe off, more gel padding was used to get a clear scan.

The second component of this investigation focused on validating the load cells embedded within the Ultrashoe. Initially, the load cells were calibrated by applying known loads through an Instron machine and adjusting a conversion factor in post-processing. When the load cells were tested in parallel, they demonstrated minimal error (<0.5%). When incorporated into the Ultrashoe housing, this error increased slightly (~1%) and further when tested within the fully assembled Ultrashoe (<2%). It was noted that the forefoot errors were higher than the heel errors, and this could be attributed to one or more of the load cells being misaligned during the testing procedure. Additionally, a slight delay (~25 ms) was observed between the load applied by the Instron and the force recorded by the load cells. The source of this delay is thought to be due to either the material of the Ultrashoe, urethane rubber, which is viscoelastic, or a slight delay in the electrical outputs from the Instron load cell compared to the load cells inside the Ultrashoe. This delay was considered acceptable and not likely to impact the performance of the Ultrashoe in practical applications. However, a subsequent investigation into the forefoot needs to be done to ensure that the high errors in the forefoot are not always present. Overall, the load cells provided accurate and reliable force measurements.

One factor that was not examined is whether some of the force measured by the load cells bypasses the ultrasound probe. The stiffness calculation assumes that the measured force directly corresponds to the force causing deformation. However, it is possible that during compression, part of the load captured by the load cells does not act on the ultrasound probe itself. This may be due to the large surface area of the heel and the way pressure is distributed across the Ultrashoe's sole, causing the load cells to detect forces outside the probe's contact region.

In LabVIEW, the DAQ was configured to sample at 1000 Hz and read 100 samples per loop, meaning it should have collected 100 samples every 0.1 seconds. However, it is believed that the specified sampling rate of 1000 Hz was below the minimum sampling rate for the hardware used and this caused the sampling rate to be inflated to the next highest available sampling rate. This did not deteriorate the quality of the data and the primary downside was having an odd and non-integer sampling rate of 1612.90 Hz.

The third inquiry involved using the Ultrashoe with a cadaveric foot to apply cyclic loading through the tibia, thereby compressing the heel pad tissue and enabling stiffness calculations. Previous iterations of the Ultrashoe were tested on human subjects. In the first version, an ultrasound probe was embedded in a commercial shoe, while a plantar pressure sensor was placed contralaterally to estimate loading. Although effective, this setup presented a limitation in that the measured force and deformation were derived at the same location, but between different trials. The second iteration addressed this by integrating load cells in series with the ultrasound probe and using additive manufacturing to develop a custom shoe. The third iteration, used in this thesis, further refined the design by implementing molding techniques for shoe and component fabrication. This enhanced user comfort, enabled using shoes of various sizes, and improved safety for diabetic populations from the padding on the straps. Although iterations two and three were tested with patients (data not included as part of this master's thesis), development was paused due to damage to the ultrasound probe's wiring. The current work advanced the understanding of the Ultrashoe by validating its embedded sensors and demonstrating that it can reliably calculate tissue stiffness under controlled experimental conditions. While cadaveric tissue offers a useful

approximation of in vivo mechanical behavior, the purpose of this inquiry was to foremost demonstrate the efficacy of the Ultrashoe to calculate stiffness.

Additionally, repeated loading during conditioning cycles may alter the effective, aggregate speed of sound of plantar tissue. The optimal speed of sound identified in this study was based on tissue that was not preconditioned and may not reflect changes that occur after preconditioning. During dynamic gait trials, the relative position of the foot with respect to the fixed probe can shift mediolaterally and anteroposteriorly, meaning consecutive steps may not image the exact same tissue path. This spatial ambiguity introduces frame-to-frame variability and represents a limitation in using ultrasound for gait analysis. While likely unmitigable, one approach to addressing this would be to measure deformation at the heel and second metatarsal head mediolaterally and assess the sensitivity of stiffness measurements to probe position using further cadaveric studies. Although implementing a registration process to track probe position would be complex, it may be a worthwhile direction for future research. It is hypothesized that the effects of minor probe shifts are minimal, particularly when tissue is properly preconditioned, but this remains an important area for further investigation.

Stiffness was estimated in this study by aligning the peaks of the force and deformation curves, a method that introduces some temporal inaccuracy. Although this does not precisely represent the true timing of loading with respect to the deformation, it was deemed necessary for estimating stiffness. Discrepancies may also exist between the force applied via the Instron and that measured by the load cells due to alternative load paths. For example, when the foot contacts both the ultrasound probe and the surrounding platform, a portion of the load may bypass the probe and be

directly transmitted to the load cells. This introduces uncertainty in stress calculations, particularly if stress is normalized by the probe's contact area without accounting for diverted load. Since the proportion of load that bypasses the probe is currently unquantified, stress-based metrics remain uncertain. In contrast, strain measurements are unaffected by this issue and can be reliably reported. For these reasons, stiffness was selected as the primary metric of interest for Ultrashoe applications, rather than presenting the elastic modulus.

Two stiffness metrics were used in this analysis: the peak-to-trough slope and a linear fit applied to the final portion of the loading curve. While the linear fit generally produced slightly higher stiffness values, consistent with expectations for targeting the linear elastic region, it also exhibited greater variability across samples compared to the peak-to-trough method. The fit stiffness is theoretically a more accurate representation of tissue stiffness due to its focus on the presumed linear region of the force-deformation curve. However, there likely needed to be more force applied to consistently fit the curve on solely samples inside this linear elastic region. In future use of the Ultrashoe, the loading during walking will greatly exceed the 200N applied to the tibia (with <100 N being registered by the load cells) and is assumed to push the tissue into this region for a more accurate fit stiffness metric. Peak-to-trough method was intended to represent how strain elastography is implemented clinically, however, in strain elastography there is an associated strain map for the tissue before and after compression. Future work should seek to utilize calculating the displacement across the whole ultrasound image to create displacement maps during stance phase to further expand the analysis from using just the closest skin to bone point to looking at all the tissue being analyzed, specifically looking at macrochamber and microchamber mechanical differences and potential changes due to diabetes.

Manual labeling of ultrasound images remains a significant limitation due to the time burden and potential for user error. Identifying anatomical landmarks such as the calcaneus and skin in each frame is a source of variability between labelers and sessions. In this work, all labeling was performed by a single individual, and due to time constraints, no intraclass correlation coefficient analysis was conducted to assess reliability. A possible solution to the intensive labeling process is the implementation of machine learning to automate the segmentation of the bone and skin. By training a model on manually segmented ultrasound images, it could be possible to automate the detection of anatomical boundaries (i.e., skin, calcaneus, second metatarsal head) across large datasets, improving efficiency and reproducibility. This advancement would further support the broader integration of the Ultrashoe into research workflows.

Finally, the current Ultrashoe design has mechanical limitations. The ultrasound probe used in this study is custom-ordered and disassembled from its housing to fit within the device, resulting in exposed wiring that exits laterally from the shoe. This wiring is vulnerable to damage during walking. In previous trials, the probe wiring failed after short bouts of treadmill use, interrupting further testing (Figure 27).

Figure 27: Broken ultrasound probe.

Given the high cost and custom nature of these probes, future iterations of the Ultrashoe should incorporate design improvements to protect (i.e., strain relieve) the wiring and increase its durability. Additionally, the mechanical load tolerance of the probe itself is not well understood, as it is not designed to withstand substantial compressive forces. Although loads applied in this study were limited to a maximum of 250 N, it is essential to characterize the probe's failure threshold to ensure safe and effective use in future applications.

Conclusions

This work focused on the validation of the sensors of the Ultrashoe and sought to demonstrate its efficacy in calculating stiffness of the plantar soft tissue underneath the heel in a cadaveric foot. The most accurate speeds of sound (available to our ultrasound device) for the plantar soft tissue

in the heel (1600 m/s) and the second metatarsal head (1660 m/s) were identified. The load cells in the Ultrashoe showed less than 2% of error for loads applied through the probe head, with greater errors in the forefoot than the heel. And finally, the Ultrashoe was demonstrated to be able to be used to calculate stiffness in cadaveric tissue using a simple method of estimating it quasi-statically as well as a more specific method of fitting a curve to the last 50% of the loading curve. The fit stiffness method resulted in a typically higher and more variable estimated stiffness calculation than the simple peak-to-trough stiffness. Additionally, it was shown that the measured stiffness increases with frequency and decreases with increased assumed speed of sound. Future work should seek to implement the Ultrashoe in subjects with diabetes to investigate any potential differences compared to healthy subjects, implement hardware updates to make it more durable, and sophisticate the analysis pipeline to reduce user input and improve reliability. This work represents the precursor validation process to using the Ultrashoe in studies to investigate the structural changes in the foot that occur to diabetes and explore its use in conjunction with plantar pressure readings.

References

[1] “International Diabetes Federation. IDF Diabetes Atlas, 11th edn. Brussels, Belgium: International Diabetes Federation, 2025.”

[2] “Centers for Disease Control and Prevention. National Diabetes Statistics Report website. https://www.cdc.gov/diabetes/data/statistics-report/index.html. Accessed May 10, 2025.”

[3] “Emily D. Parker, Janice Lin, Troy Mahoney, Nwanneamaka Ume, Grace Yang, Robert A. Gabbay, Nuha A. ElSayed, Raveendhara R. Bannuru; Economic Costs of Diabetes in the U.S. in 2022. Diabetes Care 2 January 2024; 47 (1): 26–43. https://doi.org/10.2337/dci23-0085.”

[4] “U.S. Department of Veterans Affairs, Office of Research & Development, ‘Diabetes,’ VA Research, [Online]. Available: https://www.research.va.gov/topics/diabetes.cfm. [Accessed: May 20, 2025].”

[5] “American Diabetes Association, ‘Standards of Care in Diabetes—2023,’ Diabetes Care, vol. 46, suppl. 1, pp. S1–S291, Jan. 2023. doi: 10.2337/dc23-S001.”.

[6] J. M. Trujillo, W. Nuffer, and S. L. Ellis, “GLP-1 receptor agonists: a review of head-to-head clinical studies,” *Therapeutic Advances in Endocrinology*, vol. 6, no. 1, pp. 19–28, Feb. 2015, doi: 10.1177/2042018814559725.

[7] K. Hamed *et al.*, “Glucagon-Like Peptide-1 (GLP-1) Receptor Agonists: Exploring Their Impact on Diabetes, Obesity, and Cardiovascular Health Through a Comprehensive Literature Review,” *Cureus*, Sep. 2024, doi: 10.7759/cureus.68390.

[8] S. A. Bus *et al.*, “Guidelines on the prevention of foot ulcers in persons with diabetes (IWGDF 2019 update),” *Diabetes Metabolism Res*, vol. 36, no. S1, p. e3269, Mar. 2020, doi: 10.1002/dmrr.3269.

[9] G. E. Reiber, R. E. Pecoraro, and T. D. Koepsell, “Risk Factors for Amputation in Patients with Diabetes Mellitus: A Case-Control Study,” *Ann Intern Med*, vol. 117, no. 2, pp. 97–105, Jul. 1992, doi: 10.7326/0003-4819-117-2-97.

[10] L. Delbridge, G. Ctercteko, C. Fowler, T. S. Reeve, and L. P. Le Quesne, “The aetiology of diabetic neuropathic ulceration of the foot,” *Journal of British Surgery*, vol. 72, no. 1, pp. 1–6, Jan. 1985, doi: 10.1002/bjs.1800720102.

[11] A. Gefen, “Plantar soft tissue loading under the medial metatarsals in the standing diabetic foot,” *Medical Engineering & Physics*, vol. 25, no. 6, pp. 491–499, Jul. 2003, doi: 10.1016/S1350-4533(03)00029-8.

[12] W. R. Ledoux, J. B. Shofer, M. S. Cowley, J. H. Ahroni, V. Cohen, and E. J. Boyko, “Diabetic foot ulcer incidence in relation to plantar pressure magnitude and measurement location,” *Journal of Diabetes and its Complications*, vol. 27, no. 6, pp. 621–626, Nov. 2013, doi: 10.1016/j.jdiacomp.2013.07.004.

[13] “A. J. M. Boulton and R. W. Whitehouse, ‘The Diabetic Foot,’ in Endotext, K. R. Feingold, B. Anawalt, A. Boyce, et al., Eds. South Dartmouth, MA: MDText.com, Inc., 2000. [Online]. Available: https://www.ncbi.nlm.nih.gov/books/NBK409609/ [Accessed: May 20, 2025].”.

[14] W. R. Ledoux and S. Telfer, Eds., *Foot and ankle biomechanics*. Amsterdam: Academic Press, 2023. doi: 10.1016/C2017-0-03286-X.

[15] K. E. Chatwin, C. A. Abbott, A. J. M. Boulton, F. L. Bowling, and N. D. Reeves, “The role of foot pressure measurement in the prediction and prevention of diabetic foot ulceration—A comprehensive review,” *Diabetes Metabolism Res*, vol. 36, no. 4, p. e3258, May 2020, doi: 10.1002/dmrr.3258.

[16] W. R. Buschmann, M. H. Jahss, F. Kummer, P. Desai, R. O. Gee, and J. L. Ricci, “Histology and Histomorphometric Analysis of the Normal and Atrophic Heel Fat Pad,” *Foot Ankle Int.*, vol. 16, no. 5, pp. 254–258, May 1995, doi: 10.1177/107110079501600502.

[17] C.-C. Hsu *et al.*, “Diabetic effects on microchambers and macrochambers tissue properties in human heel pads,” *Clinical Biomechanics*, vol. 24, no. 8, pp. 682–686, Oct. 2009, doi: 10.1016/j.clinbiomech.2009.06.005.

[18] M. S. P. Huijberts, N. C. Schaper, and C. G. Schalkwijk, “Advanced glycation end products and diabetic foot disease,” *Diabetes Metab. Res. Rev.*, vol. 24, no. S1, pp. S19–S24, May 2008, doi: 10.1002/dmrr.861.

[19] J. C. Teoh and T. Lee, “Assessment of tissue glycation on plantar soft tissue stiffness,” *Journal of Foot and Ankle Research*, vol. 7, no. S1, p. A83, Jan. 2014, doi: 10.1186/1757-1146-7-S1-A83.

[20] S. A. Bus, M. Maas, and R. Lindeboom, “Reproducibility of foot structure measurements in neuropathic diabetic patients using magnetic resonance imaging,” *Magnetic Resonance Imaging*, vol. 24, no. 1, pp. 25–32, Jul. 2006, doi: 10.1002/jmri.20601.

[21] S. Dalal, A. D. Widgerow, and G. R. Evans, “The plantar fat pad and the diabetic foot – a review,” *International Wound Journal*, vol. 12, no. 6, pp. 636–640, Dec. 2015, doi: 10.1111/iwj.12173.

[22] S. Harish C, R. Dixit, S. Singh, and S. Garg, “Sonoelastographic Evaluation of the Achilles Tendon in Patients With Type 2 Diabetes Mellitus,” *Ultrasound in Medicine & Biology*, vol. 46, no. 11, pp. 2989–2997, Nov. 2020, doi: 10.1016/j.ultrasmedbio.2020.07.023.

[23] S. Harish C., R. Dixit, S. Singh, and S. Garg, “Evaluation of the plantar fascia in patients with diabetes mellitus: the role of sonoelastography,” *Pol J Radiol*, vol. 87, pp. 500–505, Sep. 2022, doi: 10.5114/pjr.2022.119474.

[24] T. Kimura, E. D. Thorhauer, M. W. Kindig, J. B. Shofer, B. J. Sangeorzan, and W. R. Ledoux, “Neuropathy, claw toes, intrinsic muscle volume, and plantar aponeurosis thickness in diabetic feet,” *BMC Musculoskelet Disord*, vol. 21, no. 1, p. 485, Dec. 2020, doi: 10.1186/s12891-020-03503-y.

[25] C. W. Hicks, D. Wang, B. G. Windham, K. Matsushita, and E. Selvin, “Prevalence of peripheral neuropathy defined by monofilament insensitivity in middle-aged and older adults in two US cohorts,” *Sci Rep*, vol. 11, no. 1, p. 19159, Sep. 2021, doi: 10.1038/s41598-021-98565-w.

[26] C. W. Hicks and E. Selvin, “Epidemiology of Peripheral Neuropathy and Lower Extremity Disease in Diabetes,” *Curr Diab Rep*, vol. 19, no. 10, p. 86, Oct. 2019, doi: 10.1007/s11892-019-1212-8.

[27] S. A. Bus *et al.*, “Footwear and offloading interventions to prevent and heal foot ulcers and reduce plantar pressure in patients with diabetes: a systematic review,” *Diabetes Metabolism Res*, vol. 32, no. S1, pp. 99–118, Jan. 2016, doi: 10.1002/dmrr.2702.

[28] L. E. Vossen, S. A. Bus, and J. J. Van Netten, “Unlocking the multidimensionality of plantar pressure measurements for the evaluation of footwear in people with diabetes,”

Journal of Biomechanics, vol. 180, p. 112502, Feb. 2025, doi: 10.1016/j.jbiomech.2025.112502.

[29] S. Wild, G. Roglic, A. Green, R. Sicree, and H. King, "Global Prevalence of Diabetes," *Diabetes Care*, vol. 27, no. 5, pp. 1047–1053, May 2004, doi: 10.2337/diacare.27.5.1047.

[30] X. Yang, Z. Peng, X. Liu, X. Liu, and S. Lu, "A narrative review of the measurement methods for biomechanical properties of plantar soft tissue in patients with diabetic foot," *Front. Endocrinol.*, vol. 15, p. 1332032, Jul. 2024, doi: 10.3389/fendo.2024.1332032.

[31] F. Draghi, S. Gitto, C. Bortolotto, A. G. Draghi, and G. Ori Belometti, "Imaging of plantar fascia disorders: findings on plain radiography, ultrasound and magnetic resonance imaging," *Insights Imaging*, vol. 8, no. 1, pp. 69–78, Feb. 2017, doi: 10.1007/s13244-016-0533-2.

[32] G. Dean Deyle, "The role of MRI in musculoskeletal practice: a clinical perspective," *Journal of Manual & Manipulative Therapy*, vol. 19, no. 3, pp. 152–161, Aug. 2011, doi: 10.1179/2042618611Y.0000000009.

[33] A. B. Rosskopf, C. Loupatatzis, C. W. A. Pfirrmann, T. Böni, and M. C. Berli, "The Charcot foot: a pictorial review," *Insights Imaging*, vol. 10, no. 1, p. 77, Dec. 2019, doi: 10.1186/s13244-019-0768-9.

[34] M. Mischi, N. G. Rognin, and M. A. Averkiou, "Ultrasound Imaging Modalities," in *Comprehensive Biomedical Physics*, Elsevier, 2014, pp. 361–385. doi: 10.1016/B978-0-444-53632-7.00217-3.

[35] S. A. Goss, R. L. Johnston, and F. Dunn, “Compilation of empirical ultrasonic properties of mammalian tissues. II,” *The Journal of the Acoustical Society of America*, vol. 68, no. 1, pp. 93–108, Jul. 1980, doi: 10.1121/1.384509.

[36] C. Dietrich *et al.*, “Strain Elastography - How To Do It?,” *Ultrasound Int Open*, vol. 03, no. 04, pp. E137–E149, Sep. 2017, doi: 10.1055/s-0043-119412.

[37] M. S. Taljanovic *et al.*, “Shear-Wave Elastography: Basic Physics and Musculoskeletal Applications,” *RadioGraphics*, vol. 37, no. 3, pp. 855–870, May 2017, doi: 10.1148/rg.2017160116.

[38] A. Sabatino *et al.*, “Validation by CT scan of quadriceps muscle thickness measurement by ultrasound in acute kidney injury,” *J Nephrol*, vol. 33, no. 1, pp. 109–117, Feb. 2020, doi: 10.1007/s40620-019-00659-2.

[39] S. D. Steppacher, M. S. Hanke, C. A. Zurmühle, P. C. Haefeli, F. M. Klenke, and M. Tannast, “Ultrasonic cartilage thickness measurement is accurate, reproducible, and reliable—validation study using contrast-enhanced micro-CT,” *J Orthop Surg Res*, vol. 14, no. 1, p. 67, Dec. 2019, doi: 10.1186/s13018-019-1099-8.

[40] F. Mechelli, L. Arendt-Nielsen, M. Stokes, and S. Agyapong-Badu, “Validity of Ultrasound Imaging Versus Magnetic Resonance Imaging for Measuring Anterior Thigh Muscle, Subcutaneous Fat, and Fascia Thickness,” *MPs*, vol. 2, no. 3, p. 58, Jul. 2019, doi: 10.3390/mps2030058.

[41] M. Shi, T. Vercauteren, and W. Xia, “Learning-based sound speed estimation and aberration correction for linear-array photoacoustic imaging,” *Photoacoustics*, vol. 38, p. 100621, Aug. 2024, doi: 10.1016/j.pacs.2024.100621.

[42] “T. C. Huynh, ‘Instrumented Footwear to Measure Plantar Tissue Properties,’ M.S. thesis, Dept. of Mechanical Engineering, University of Wasington, 2020. [Online]. Available: ProQuest Dissertations & Theses.”.

[43] S. Telfer, J. Woodburn, and D. E. Turner, “Measurement of functional heel pad behaviour in-shoe during gait using orthotic embedded ultrasonography,” *Gait & Posture*, vol. 39, no. 1, pp. 328–332, Jan. 2014, doi: 10.1016/j.gaitpost.2013.07.118.

[44] *Mimics. Materialise Inc. (25.1 ed.)*.

[45] *M. Musy et al., “vedo, a python module for scientific analysis and visualization of 3D objects and point clouds”, Zenodo, 10.5281/zenodo.2561401.*

[46] I. I. Geneva, B. Cuzzo, T. Fazili, and W. Javaid, “Normal Body Temperature: A Systematic Review,” *Open Forum Infectious Diseases*, vol. 6, no. 4, p. ofz032, Apr. 2019, doi: 10.1093/ofid/ofz032.

[47] E. D. Thorhauer, C. Wukelic, N. Entress, J. B. Shofer, and W. R. Ledoux, “Verifying the accuracy and precision of foot bone segmentation from fan beam and cone beam computed tomography scans,” *Medical Engineering & Physics*, vol. 140, p. 104349, Jun. 2025, doi: 10.1016/j.medengphy.2025.104349.